ISTANBUL TECHNICAL UNIVERSITY ★ GRADUATE SCHOOL OF SCIENCE ENGINEERING AND TECHNOLOGY

INFLUENCE OF STATIC TORSION ON THE MECHANICAL PROPERTIES OF HEAVILY DRAWN STEEL WIRES

M.Sc. THESIS

Gökay BARANOĞLU

Department of Metallurgical and Materials Engineering

Materials Engineering Programme

AUGUST 2012

ISTANBUL TECHNICAL UNIVERSITY ★ GRADUATE SCHOOL OF SCIENCE ENGINEERING AND TECHNOLOGY

INFLUENCE OF STATIC TORSION ON THE MECHANICAL PROPERTIES OF HEAVILY DRAWN STEEL WIRES

M.Sc. THESIS

Gökay BARANOĞLU
(506101412)

Department of Metallurgical and Materials Engineering

Materials Engineering Programme

Thesis Advisor: Prof. Dr. E.Sabri KAYALI

AUGUST 2012

<u>İSTANBUL TEKNİK ÜNİVERSİTESİ ★ FEN BİLİMLERİ ENSTİTÜSÜ</u>

STATİK BURMANIN AŞIRI ÇEKİLMİŞ ÇELİK TELLERİN MEKANİK ÖZELLİKLERİNE ETKİSİ

YÜKSEK LİSANS TEZİ

Gökay BARANOĞLU
(506101412)

Metalurji ve Malzeme Mühendisliği Anabilim Dalı

Malzeme Mühendisliği Programı

Tez Danışmanı: Prof. Dr. E.Sabri KAYALI

AĞUSTOS 2012

Gökay BARANOĞLU, a **M.Sc.** student of ITU **Institute of Science Engineering and Technology** student ID 506101412, successfully defended the thesis entitled "Influence of static torsion on the mechanical properties of heavily drawn steel wires", which he prepared after fulfilling the requirements specified in the associated legislations, before the jury whose signatures are below.

Thesis Advisor :	**Prof. Dr. E. Sabri KAYALI** Istanbul Technical University	....
Jury Members :	**Prof. Dr. Hüseyin ÇİMENOĞLU** Istanbul Technical University	....
	Assoc.Prof. Dr. Erdem ATAR Gebze Institute of High Technology	....

FOREWORD

This thesis has been done in K.U.Leuven with collaboration Istanbul Technical University during my erasmus programme. Prof. Dr. Bert Verlinden and Prof. Dr. Martine Wevers has supervised my thesis during my erasmus programme in K.U.Leuven.

I'm highly indebted to my supervisors, Prof. Dr. E. Sabri Kayalı, Prof. Dr. Bert Verlinden and Prof. Dr. Martine Wevers for their good guidance and constant supervison as well as for providing necessary information regarding the thesis and also for their support in completing the master thesis.

I would also like to express my gratitude towards Assoc. Prof. Dr Murat Baydoğan and Kobe Thys for their help during my first experimentals.

I would like to express my special thanks and gratitude to K.U.Leuven and ITU persons for giving me such attention and time. My thanks and appreciations also go to my colleagues in developing the thesis and people who willingly helped me out with their abilities.

August 2012

Gökay BARANOĞLU
(Material Engineer)

TABLE OF CONTENTS

Page

ABBREVIATIONS

APFIM	:Atom probe field ion microscopy
EBSD	:Electron backscatter diffraction
FCG	:Fatigue crack growth
FCT	:The facet area
FGA	:Fine granular area
GFA	:Granular bright facet
HV	:Vickers hardness
LCF	:Low cycle fatigue
ODA	:Optical dark area
UTS	:Ultimate tensile strength
SEM	:Scanning electron microscope
TEM	:Transmission electron microscope
VHCF	:Very high cycle fatigue

LIST OF TABLES

Page

LIST OF FIGURES

Page

INFLUENCE OF STATIC TORSION ON THE MECHANICAL PROPERTIES OF HEAVILY DRAWN STEEL WIRES

SUMMARY

The influence of static torsion on the mechanical behavior such as tensile, hardness and fatigue behavior of heavily drawn steel wires with a diameter of 175 μm has been studied. The heavily drawn steel wires have been successfully used as reinforcement for truck&bus tires for their high strength with acceptable level of ductility. The steel wires are bundled to steel cords which are processed in the rubber. A certain steady torsion is applied to steel wires during bundling and when the vehicle starts moving a dynamic load is superimposed on the static load. This means a combination of constant mode III load with a cyclic mode I load in the fracture mechanics.

It is generally agreed today that the torsion would cause a retardation of the growth rate of surface cracks, leading to a higher probability of failure by internal crack growth for motor shafts. The purpose of this thesis to determine if this effect is also applicable to steel wire filaments.

Wire drawing is a metal-working process used to reduce the cross-sectional area of a wire by pulling it through single, or series of drawing die(s) (Figure 2.1). Drawing is usually performed at room temperature, thus classified as a cold working process, but it may be performed at elevated temperatures for large wires to reduce forces. After the cold working process, a long product is produced with constant cross section that has an excellent surface finish and controlled dimensions.

Patenting consists of passing the wire through tubes in a furnace at a temperature in the austenite region, usually 950-1000 °C. This high temperature treatment produces uniform austenite of rather large grain size. The wire is then cooled rapidly in air or molten lead for a period of time so that the resulting structure consists of very fine pearlite preferably with no seperation of primary ferrite.

The brass coating process ,which has a two-fold function namely lubrication and adhesion, is usually done before wet wire drawing (the wires that were investigated in this study are brass coated steel wires). Brass coating acts as some kind of lubricant during the wet wire drawing process because it is much softer than the steel wire itself. The brass coating reacts with the sulfur in the rubber to obtain a strong interlocking between rubber and the steel wire and this adhesion is very important when the steel wire is used as steel cord in tire applications.

It is important to clean the wires by wiping the surface at least 5 times with acetone to remove the dirt and residual lubricant, followed by wiping the surface at least 2 times with ethanol to remove the residual acetone. The glue reacts with the water that is present at the surface of the wire. Both of the cleaning operation before the coating and the reaction between the glue and the water (corrosion is impossible without water) improves the fatigue lives of the steel wire.

Based on the tensile test results, the tensile strength decreased and the ductility increased in correlation with an increased of the amount of torsion. This finding is consistent with the literature, because the plastic flow is relatively unconstrained in torsion and creates the large plastic zone at the crack tip prior to fracture. Therefore, the contribution of mode III leads a higher fracture toughness than pure mode I.

According to the hardness test results, the hardness values that were measured are not consistent and are not proportional with the torsional deformation. Due to inhomogenous cementite decomposition of steel wire during drawing, the torsional deformation does not propagate easily in a steel wire and tends to accumulate locally. Therefore, this fact may be one of the reason why the hardness values are not consistent for the steel wire.

Based on experimental fatigue data two different fracture modes namely surface and internal fatigue crack inititaions are active for heavily drawn steel wires under pure mode I and mixed mode I+III. When the sample subjected to twisting 2 times, no torsion effect was observed on the fatigue properties compared to pure mode I. However, the number of cycles (fatigue lives) of the samples decreased when the number of rotations were more than 2 times.

Only cracks that initiated from the surface leading to low cycle fatigue lives were found. Enviromental interaction can have an effect on surface crack inititaions, therefore surface crack inititaions are most critical mechanisms for the steel wire. No internal cracks were observed in sample with more than 2 twists. A characteristic area namely the optically dark area was observed on the fracture surface of the sample which fractured internally. No enviromentally assisted crack initiation affects this internal fracture mode, because the fatigue crack is located completely inside the metal.

Steel wires that used as reinforcement for truck and bus should be twisted less due to increasing strength and fatigue lives. I believe that my study serves as a window to an investigating of the reasons why the torsion effect which has been described for shafts is not acceptable to the fatigue properties of heavily drawn steel wires.

STATİK BURMANIN AŞIRI ÇEKİLMİŞ ÇELİK TELLERİN MEKANİK ÖZELLİKLERİNE ETKİSİ

ÖZET

Özellikle otomotiv endüstrisinde kullanılan çelik tellerin kimyasal kompozisyonu ötektoid olup, mikroyapı ise ferrit ve sementitden oluşmaktadır. Dolayısıyla bu endüstride kullanılan aşırı çekilmiş çelik teller sahip oldukları perlitik mikroyapı sonucu kazandıkları yüksek dayanımları ve beraberindeki kabul edilebilir seviyedeki süneklikleriyle kamyon ve otobüs lastikleri için takviye malzemesi olarak başarılı şekilde kullanılmaktadır.

Çelik teller birbirlerine burularak kauçuk içindeki çelik korda tutturulur. Burma sırasında çelik teller üzerinde statik burma yüklemesi etkili olurken, araç hareket etmeye başladığında bu statik yüklemenin üzerine dinamik yükleme binmektedir. Bu durum literatürde kırılma mekaniği konusu için sabit yükleme mod III ile değişken yükleme mod I'in kombinasyonu olarak bilinmektedir.

Literatürde, miller üzerinde etkili olan burulmanın çalışma koşullarında nasıl etki ettiği araştırılmıştır. Statik burma etkisinin millerde çatlak başlangıcı ve son kırılma arasında geçen süreyi uzattığı günümüzde kabul gören bir gerçektir. Burma yüzey çatlaklarının büyüme hızında gecikmeye yol açmış ve malzemenin iç çatlaklardan kırılmasına doğru yönelttiği belirlenmiştir.

Yüzey kırılmasından ziyade iç yapıdan kırılan malzemenin yorulma ömrünün daha uzun olduğu gerçeğini göz önünde bulundurursak, miller üzerinde statik burmanın mod I+ III yükleme koşullarında yorulma ömürlerini arttırdığını söyleyebiliriz. Bu tezin genel amacı miller üzerinde etkili olan bu burma etkisinin çelik teller üzerinde başta yorulma davaranışı olmak üzere diğer çekme testi ve sertlik testi sonucunda elde edilen mekanik davranışlarında da etkili olup olmadığının araştırılmasıdır.

Çalışmada öncelikle çelik tellerin üretim prosesi, proses esnasında mikroyapıdaki değişimler anlatılmıştır. Daha sonrasında ise çalışmada yapılan mekanik testler ve sonuçları ele alınmıştır.

Bu çalışmada, 175 µm çapındaki pirinç kaplamalı aşırı çekilmiş çelik teller üzerindeki statik burma etkisinin malzemede çekme, sertlik ve yorulma gibi mühendislik testlerinden elde edilen mekanik davranışlarına etkisi araştırılmıştır.

Tel çekme işlemi filmaşin adı verilen büyük çaptaki tellerin kalıplar arasından çekilerek daha küçük çap haline getirme işlemidir. Tel çekme işlemi oda sıcaklığında yapıldığından soğuk işlem olarak adlandırılır. Tel çekme işlemi sonucunda daha iyi malzeme özelliklerine ve mükemmel yüzey özelliklerine sahip uzun ürünler elde edilir. Malzemedeki pekleşmeyi önlemek amacıyla tavlama ısıl işlemi gerekebilir.

Çelik tellerde arzu edilen ince perlit mikroyapısnı elde etmek amacıyla patentleme ısıl işlemi yapılmaktadır. Patentleme ısıl işlemi çelik teli öncelikle östenit sıcaklığına

kadar ısıtmak ardından havada ya da banyolarda hızlı bir şekilde soğutma işlemlerini kapsamaktadır.

Otomotiv endüstrisinde kullanılacak çelik teller için bir diğer önemli proses çelik yüzeyini pirinç kaplamaktır. Pirinç kaplama işleminin yapışma ve yağlama olmak üzere başlıca iki fonksiyonu vardır. Pirinç çeliğin kendisinden daha yumuşak olduğu için kaplama işlemi aynı zamanda yağlama etkisi yaparken, öte yandan da kauçuk içindeki kükürt ile reaksiyona girerek kauçuk ile çelik tel arasında kuvvetli bağlar oluşturarak yapışma görevi sağlamaktadır.

Çelik tel numunelerin mekanik test işlemlerinden önce yüzeylerinin temizlenmesi gerekir. Öncelikle çelik tel numunenin yüzeyi aseton ve ethonal ile kir ve yağı gidermek için temizlenmelidir.

Alüminyum plakalar arasında yapıştırılmış ölçme boyu 50 ±3 mm olan çelik tel numunelere çekme testi iki tip olarak uygulanmıştır. Birinci tipde numuneye statik burma yüklemesi yapılmış ardından burma yüklemesi korunarak çekme testi uygulanmıştır. İkinci tipde ise statik burma etkisinde kalan numune önce serbest bırakılmış, numunenin kendisini ne kadar geri saldığı hesaplanmış ve ardından çekme testi yapılmıştır.

Çekme testi sonuçlarına dayanarak, artan burma miktarına bağlı olarak malzemenin çekme dayanımında, akma dayanımında ve kopma yükünde azalma kopma uzamasında ise artış gözlemlenmiştir. Birinci tipteki çekme testi sonuçlarına göre malzemenin çekme ve akma dayanımı daha yüksek kopma uzaması ise düşük olarak gözlemlenmiştir. Numuneye burma etkisi yapmadan sadece çekme testi uygulandığında ise daha yüksek dayanım elde edilirken, fakat daha düşük kopma uzaması elde edilmiştir. Bu sonuçlar literaturle uyum göstermektedir, çünkü literatür araştırmasına göre burma yüklemesi sonucunda malzemede plastik akış serbest hareket etmekte ve çatlak ucunda kırılmadan önce bir plastik zon oluşturmaktadır. Bu plastik zon burma etkisiyle beraber küresel hale gelmekte ve sonuç olarak malzemenin kırılma tokluğunda artış sağlamaktadır.

Sonuç olarak, mod I+ III yükleme koşullarında gerçekleştirilen çekme testine tabi tutulan ağır çekilmiş çelik tellerde, sadece uygulanan mode I yükleme koşullarına göre daha yüksek kırılma tokluğu elde edilmektedir.

Çekme testi sonrasında kırılmış numuneler tarama elektron mikroskobunda incelenmiştir. Tarama elektron mikroskop verilerine göre kırılmış yüzeylerde sünek malzemelerle ilişkili olarak tanımlanan koni-çanak tipi kırılma ve çukurlar gözlemlenmiştir.

Çalışmada statik burmanın aşırı çekilmiş çelik tellerin sertlik özelliklerine etkisini anlayabilmek için Vickers mikro sertlik cihazı kullanılmıştır. Elde edilen sertlik test sonuçlarına göre, sertlik değerlerinin burma miktarı ile orantılı olmadığı gözlemlenmiştir.

En düşük sertlik değeri numune 20 defa buruldüğunda elde edilmiştir. Çelik tellerin çekilmesi esnasında sementit ayrışmasının homojen olmaması, burma deformasyonun çelik içerisinde tek bir yerde toplanması (kolaylıkla yayılamaması) bu durum hakkında açıklayıcı bilgiler olabilir.

Bu çalışmada yorulma testleri çekme-basma değişken yükleme koşullarında uygulanmıştır. Deneysel yorulma test verilerine dayalı olarak, bu çalışmada kullanılan aşırı çekilmiş çelik tellerde mod I ve mod I+III yükleme koşulları altında yüzey ve iç çatlak başlama mekanizmalarının yorulma davranışlarını belirlediği gözlemlenmiştir.

Yorulma test sonrasında, taramalı elektron mikroskobunda incelenen numunelerin kırılma yüzeylerinde yüzey çatlağı ve iç çatlak olmak üzere iki tip kırılma şekli gözlemlenmiştir. Yüzeyden itibaren başlayan yorulma çatlaklarında daha düşük yorulma ömürleri elde edilmiştir. Yüzey çatlaklarının yarı küresel şeklinde büyüdüğü gözlemlenmiştir. İç çatlaklarının ise küresel şeklinde büyüdüğü gözlemlenmiştir. İç çatlaklı malzeme yüzeyi incelendğinde inklüzyon çevresindeki pürüzlülüğün normal kırılma yüzeyinden daha fazla olduğu belirlenmiştir. Bu pürüzlü yüzey literatürde ‘optik karanlık yüzey’ olarak bilinmektedir. İç çatlaklı malzemelerde daha yüksek yorulma ömürleri elde edilmiştir.

Yorulma test sonuçları ve tarama elektron mikroskobunda yapılan incelemelere dayalı olarak 2 defa yapılan statik burma etkisindeki numunenin yorulma davranışı ile, hiç statik burmaya maruz bırakılmamış numunelerde yüzey ve iç çatlak başlama mekanizmaları birlikte gözlemlenmiştir. Burma miktarı 2’den fazla olan numunelere uygulanan yorulma testi sonrasında tarama elektron mikroskobunda yapılan inceleme ile hiçbir şekilde iç çatlak gözlemlenmemiş ve bu numuneler sadece yüzeyden kırılmıştır. Dolayısıyla burma sayısı 2’den fazla olduğunda daha düşük yorulma ömürleri elde edilmiştir.

Statik burma etkisin otomotiiv endüstrisinde kullanılan aşırı çekilmiş çelik tellerin hem statik hem de yorulma özelliklerine olan etkisi bu çalışmada incelenmiştir. Çalışmanın ana sonuçlarında, statik burmanın çelik tellerin statik özelliklerinde mukavemeti azalttığı ancak kopma uzamasını arttırdığı, yorulma davarnışlarında ise özellikle 2 defadan fazla burma sayılarında çok düşük yorulma ömürleri elde edildiği belirlenmiştir.

Burma miktarı malzemenin mukavemetini ve yorulma ömürlerini azalttığından dolayı daha düşük burma sayılarında malzemenin otomotiv endüstrisinde kullanılması önerilmektedir. Aynı zamanda bu çalışmanın, motor millerinde daha yüksek yorulma ömürleri neden olan burma etkisinin neden çelik teller üzerinde etkili olmadığının nedenleri konusunda yapılacak olan sonraki çalışmalara bir pencere olacağına inanmaktayım.

1. INTRODUCTION

The steel wires that will be investigated in this master thesis are brass coated steel wire filaments with a diameter of 175 μm supplied by NV Bekaert SA.

Steel wire filaments which have a diameter of 0,15-0,5 mm have been used as a reinforcement for truck&bus tires and have the highest strength of all mass-produced steel materials. The typical chemical composition of pearlitic steel wires is nearly eutectoid and the microstructure is consisting of ferrite and cementite. The steel wires are usually twisted together to form steel cords for reinforcing truck&bus tires. During twisting a certain steady torsion is applied to the filaments. When the truck or bus starts moving a dynamic load is superimposed on the static load. In the literature, this fracture mechanism has been described as a combination of constant mode III load with a cyclic mode I.

It is generally agreed today that for the shafts, when the steady torsion is superimposed to mode I, the lifetime between the crack inititaion and the final fracture is longer than that for pure mode I. The torsion would cause a retardation of the growth rate of surface cracks, leading to higher probability of failure by internal crack growth. The purpose of this thesis is to investigate if this effect is also applicable to the steel wires which are used for reinforcement of bus&truck tires.

In this thesis, first the influence of torsion on the static properties such as tensile strength and hardness of heavily drawn steel wires will be studied, then the fatigue properties will be investigated under pure mode I and mixed mode I+III.

1.1 Purpose of the Thesis

The goal of this study is to determine the influence of torsion on the mechanic properties of the steel wires which are used as reinforcement of truck&bus tires. For the purposes of this thesis, mechanical tests such as tensile test, hardness test and fatigue test with different amounts of steady torsion were performed to understand if the effect of torsion is also applicable to steel wires and what degree of the life time increases or decreases are due to steady torsion.

1.2 Approach of the Problem

The approach of the problem is shown schematically in Figure 1.1.

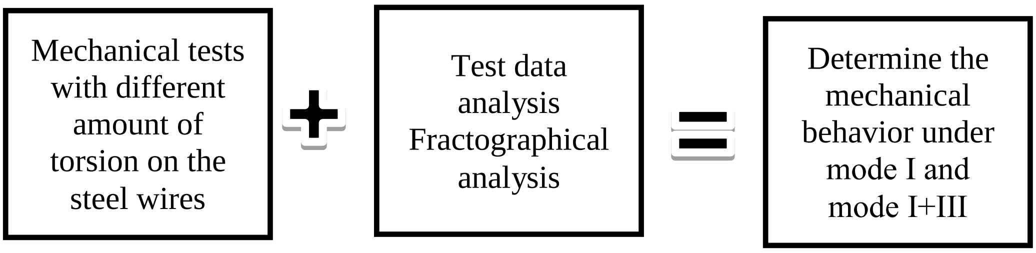

Figure 1.1: Schematic overview of the research approach

To investigate the mechanical properties of the steel wire under the mixed mode I+III, the tensile tests, hardness tests and fatigue tests are performed with different amount of torsion. Microstructural observations are obtained by scanning electron microscope (SEM). Based on the test data and fractographical analysis, the mechanical behavior of the heavily drawn steel wires under pure mode I load and mixed mode I+III load are discussed in this study.

1.3 Outline

A state of the art literature which includes the microstructural developments during wire drawing process and the mechanical behavior of heavily drawn steel wires under mode I and mixed mode I+III is given in chapter 2. Chapter 3 describes the used materials, experimental procedures and results. In chapter 4, general conclusions are given.

2. LITERATURE REVIEW

2.1 Wire Drawing Production Process

Wire drawing is a metal-working process used to reduce the cross-sectional area of a wire by pulling it through single, or series of drawing die(s) (Figure 2.1). Drawing is usually performed at room temperature, thus classified as a cold working process, but it may be performed at elevated temperatures for large wires to reduce forces. After the cold working process, a long product is produced with constant cross section that has an excellent surface finish and controlled dimensions. The process of wire drawing improves material properties due to cold working. After a number of drawing passes, annealing may be required in order to remove the effects of strain hardening before the drawing operation is continued. The pulling forces (applied at the exit of the die) and the die geometry creates a combination of tensile and compressive stresses during wire drawing process. The pulling force is limited by the strength of the wire in order to prevent any fracture or unstable deformation behaviour of steel wire. Many reductions or drawing passes should be applied in order to achieve a large overall reduction [1].

Process used in wire drawing for eutectoid steels includes following steps:

i. Chemical or mechanical descaling
ii. Dry wire drawing
iii. Patenting
iv. Brass coating
v. Wet wire drawing

The descaling process should be done to remove surface contaminants from the wire surface. This cleaning process is done by chemical pickling or mechanical descaling. Mechanical descaling by scraping and chemical pickling is done by using acid to remove the surface contaminants.

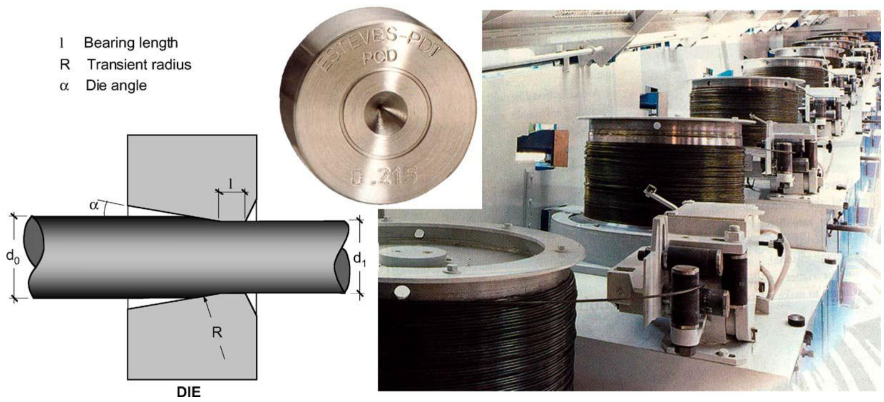

Figure 2.1: Overview of wire drawing production process [2].

If the diameter of the wire is larger than 0.5 mm and the rough surface can be acceptable, the dry drawing process is normally performed.

The patenting heat treatment is necessary to remove the effects of strain hardening. Patenting consists of passing the wire through tubes in a furnace at a temperature in the austenite region, usually 950-1000 °C. This high temperature treatment produces uniform austenite of rather large grain size. The wire is then cooled rapidly in air or molten lead for a period of time so that the resulting structure consists of very fine pearlite preferably with no seperation of primary ferrite. Successive drawing and patenting steps can be used to accomplish the desired size and strength level.

The brass coating process ,which has a two-fold function namely lubrication and adhesion, is usually done before wet wire drawing (the wires that were investigated in this study are brass coated steel wires). Brass coating acts as some kind of lubricant during the wet wire drawing process because it is much softer than the steel wire itself. The brass coating reacts with the sulfur in the rubber to obtain a strong interlocking between rubber and the steel wire and this adhesion is very important when the steel wire is used as steel cord in tire applications.

The wet drawing process is performed for wire with a diameter that is smaller than 0,5 mm in a bath of lubricant. It is important to note that the lubricant is not only chosen for its tribological properties but also for its cooling properties [1].

2.2 Microstructure of Heavily Drawn Steel Wires

Due to severe plastic deformation which is applied during wire drawing, major processes affecting microstructure of a pearlitic wire including lamellae thinning, texture changes, cementite decomposition, plastic flow localization, dynamic strain aging and residual stress development are described in the following paragraphs.

2.2.1 Lamellae thinning

X. Zhang et al. [3] investigated the microstructural evolutions of pearlitic steel wires during wet wire drawing on a very similar wire as was used in this Master project. A high strength near eutectoid steel with a carbon content of 0.7 wt.% ,which was supplied by NV Bekaert SA, was used in their study. Microstructural investigations were carried out at various steps of the overall wire drawing process from as patented wire (1.26mm) to the final drawn wire (0.20mm).

It can be seen that the cementite plates within each pearlite colony are neither parallel nor continuous (Figure 2.2A and 2.2B). X. Zhang et al. [3] suggest that the reason of this could be a high wire drawing speed which is used during the patenting process. Because of the high speed, the transformation from austenite to pearlite is completed quickly. As a result two types of pearlite can be seen in the microstructure: plate-like pearlite and particle-like pearlite. The particle-like pearlite represents a 2D-section through cementite with a rod like morphology. In some places these two types were seen in within one pearlite colony. The majority cementite is, however, of the expected plate-like morphology.

At strain 0.7, the cementite plates/particles have begun to rotate into the drawing direction. In the longitudinal section, the occurence of local shear bands were observed (Figure 2.2C). In the transverse section, the twisting is severe and break-up of the cementite plates/particles takes place (Figure 2.2D).

At strain 1,5, almost all the cementite have rotated to near drawing direction and have lengthened to such a degree that 97% of the cementite in the longitudinal section has an angle with respect to the drawing direction that is smaller than 30°. In the longitudinal section, some cracks are observed parallel to the drawing direction across cementite plates/particles (Figure 2.2E). X. Zhang et al [3] also observed that a typical ‘curled’ structure can be clearly seen in the transverse section (Figure 2.2F).

For a drawing strain of 2.7 all the cementite plates have rotated to near the drawing direction and they are greatly lengthened compared with the lower strains. In the transverse section, all the twisting of cementite is severe and the cementite plates are much thinner compared with those seen at strain 1.5 (Figure 2.2G). A typical curled pattern is obvious in the transverse section. In some places where the cementite plates/particles are comparatively long (above 1μm) shear bands are seen to develop across the cementite (inset on the right side of Figure 2.2H).

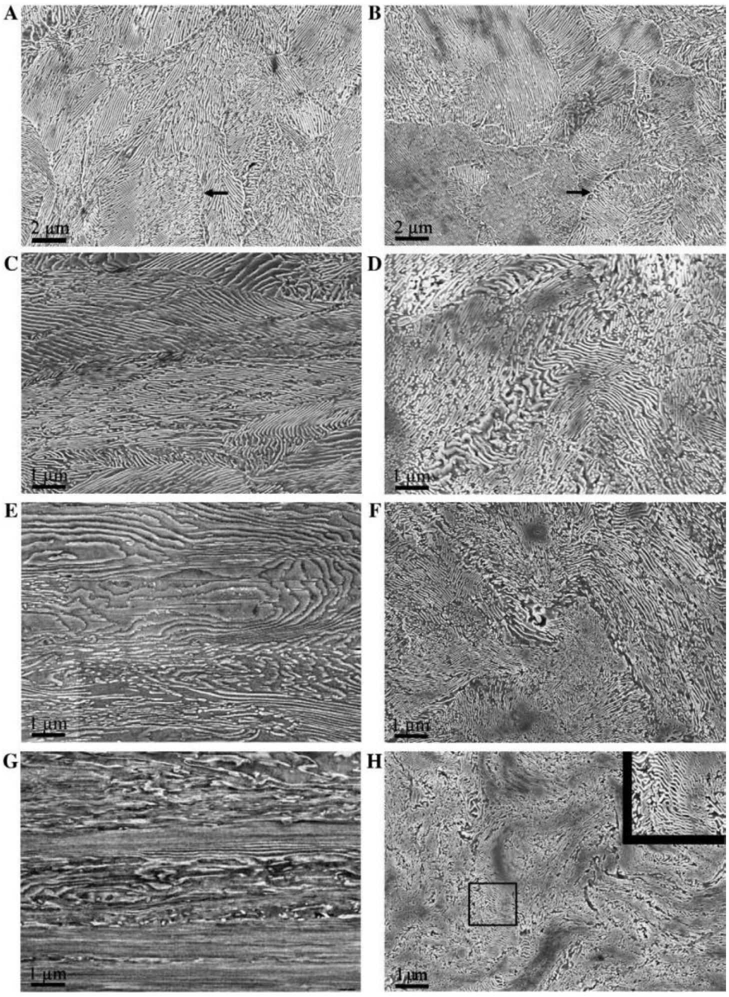

Figure 2.2: SEM images of wires deformed to different strains [3].

M. Zelin [4] investigated the evolution of the angle which characterizes the orientation of a pearlite colony with regard to the wire axis as a function of drawing strain for different original lamellae orientations for uni-axial streching law (Figure 2.3). These calculated values correspond well with the experimental observation of X. Zhang et al. [3].

The change in the thickness of cementite plates as a function of drawing strain was observed by X. Zhang et al. [3] (Figure 2.4). The experimentally measured thickness of cementite plates were obtained from transmission electron micsorcope (TEM) investigations of specimens taken from the longitudinal section and are compared in the figure with that expected at each strain from the geometrical reduction due to the change in wire diameter.

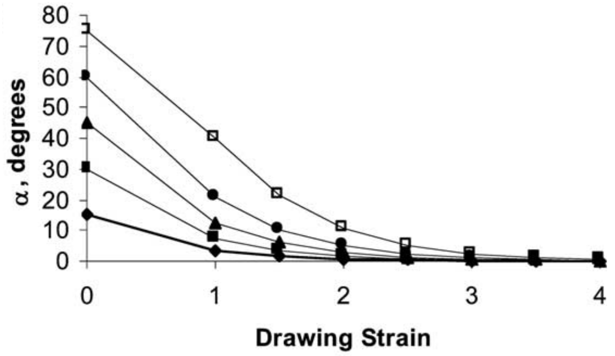

Figure 2.3: Evolution of the α-angle as a unction of drawing strain [4].

The values calculated using equation **(2.1)** under the assumption that the deformation is homogenous throughout the wire and that the cementite deforms in proportion to the drawing strain.

$$T_i = T_0 e^{-\varepsilon/2} \quad \textbf{(2.1)}$$

Where T_i *and* T_0 are cementite plate thickness at strain of 0 and i, and where ε is the strain. The average cementite plate thickness decreases from 19 nm in the as patented condition (ε=0) to 2nm at a strain of 3.7.

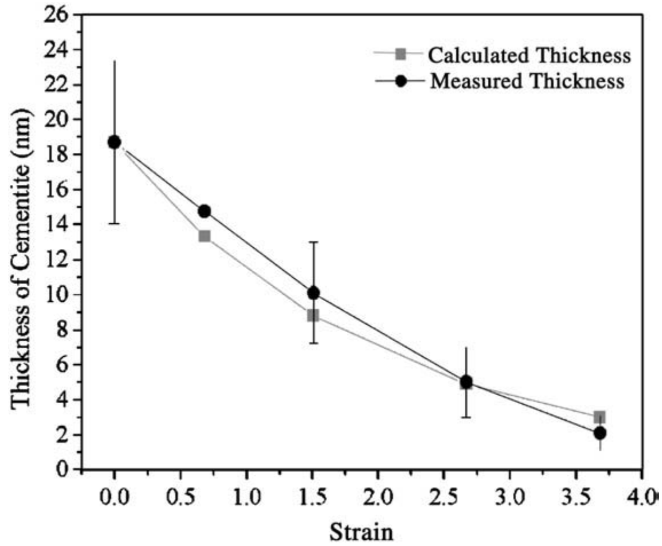

Figure 2.4: Cementite plate thickness as a function of drawing strain [3].

2.2.2 Texture changes

Two kinds of textures are formed due to the wire drawing process, namely a morphologic texture and a crystallographic texture.

It is investigated that an axial [110] texture develops during wire drawing of pearlitic steels. Due to the cold working process on the steel wire with a large diameter [5], a [110] fiber texture leads to an alignment of (001) planes, which are cleavage planes in ferrite, along the wire axis. These cleavage planes intensifies the crack propagation. Heizmann et al. [6] documented that a cyclic texture can grow in the surface layers and at the wire center and this fact can possibly improve the delamination under torsion loading.

Zelin [4] showed the effects of the crystallographic texture on the anisotropic behavior of the wire by doing micro-hardness indentations with a Knoop diamond indentor on a drawn wire (Figure 2.5). It was measured that the micro-hardness is 900 HK in the direction perpendicular to the wire axis and only 760 HK parallel to the wire axis. A large number of interlamellar interfaces prevent the dislocation movement in a normal direction as compared with axial direction acting as barriers and this fact can be the reason of the difference in micro-hardness.

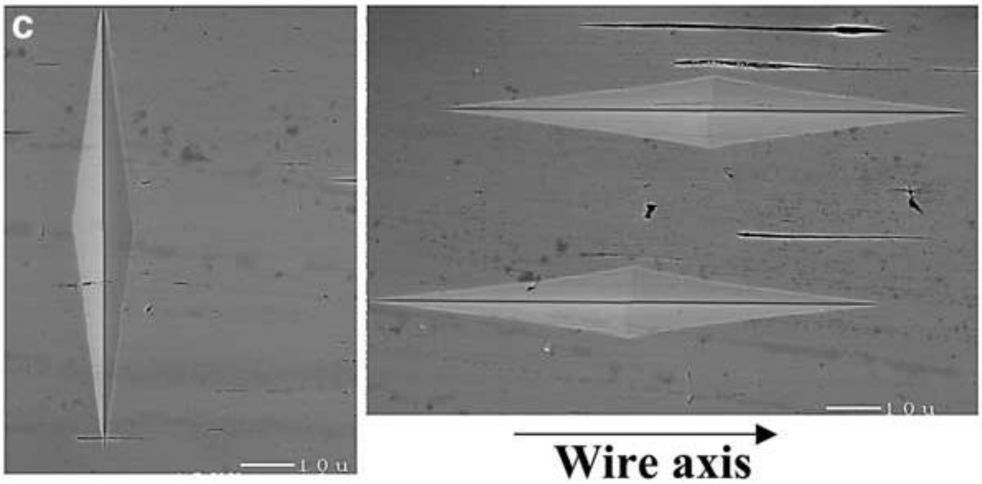

Figure 2.5: Micro-hardness indentations with a Knoop diamond [4].

2.2.3 Cementite decomposition

The authors of recent studies have proposed that it is very important to understand the evolution of cementite phase during wire drawing [3,4]. Mössbauer spectroscopy, internal friction and APFIM (atom probe field ion microscopy) are performed to investigate the mechanism of governing cementite decomposition [7,8].

The interactions between dislocations and carbon atoms in ferrite phase or the destabilization of cementite due to increase of its interfacial energy are the possible mechanisms for cementite decomposition during wire drawing. The carbon atoms move across the interface, in both mechanisms.

Most studies emphasized that the transfer of carbon atoms from cementite to dislocations accumulated near the interface controls the cementite decomposition. Gavriljuk [8] concluded that the binding enthalpy between dislocations and carbon atoms in ferrite and the interatomic bonds in cementite affect the decomposition of cementite. He also observed that the increase of the interfacial area between ferrite and cementite increases with the fraction of cementite decomposed.

Hong [9] observed that the C distribution in deformed ferrite phase is not constant and ranges from 0.2 to 3 at.%. This heterogeneous dissolution of carbon in ferrite shows that carbon is segregated to dislocations or dislocation pile-ups.

Nam et al. [10] concluded that the most probable mechanism for cementite decomposition is the interaction between dislocation and carbon atoms at the interface.

Hono et al. [11] investigated the pearlitic steel wire that was subjected to heavy cold drawing to a strain of 5.1 almost all cementite lamellae decomposed, leaving a nanoscale microstructure that is composed of ferrite fibers supersaturated with carbon. They reported that the high strength obtained in this steel wire is attributed to this structure. They also proposed the new mechanism which is based on the decomposition of cementite phase by the segregation of carbon atoms in ferrite phase.

2.2.4 Plastic flow localization

X. Zhang et al. [3] performed local SEM/EBSD measurements to understand the mechanism of the changes in the cementite plate/particle morphology during the deformation. Figure 2.6 shows the traces of the {110} and {112} slip planes in ferrite in a longitudinal section in a wire that is deformed to a strain of 0.7. The grey lines indicate pearlite colony boundaries and the white lines show the crystallographic orientations inside pearlite colonies. A schematic illustration of the deformation mechanism of the cementite is given in the right side of the figure 2.6. Trace analysis indicate that in colony A and colony C local shear bands develop that are parallel to the {110} slip plane trace in the ferrite, and that in colonies B, D and E shearing occurs in more than one direction, though in each case still parallel to either a {110} or {112} ferrite slip plane trace. It was observed that slip initiates in the ferrite lamellae and then transfered into the cementite lamellae. From the observations of coarse slip, shear bands and cracks across cementite plates/particles parallel to $\{110\}_{\alpha\text{-Fe}}$ $\{112\}_{\alpha\text{-Fe}}$ planes [3].

Zelin [4] concluded that the plastic deformation during wire drawing is not homogenous and that two systems of localized shear bands formed by coarse slip and fine slip surfaces orientated under from 30 to 45 degrees with respect to the wire axis observed.

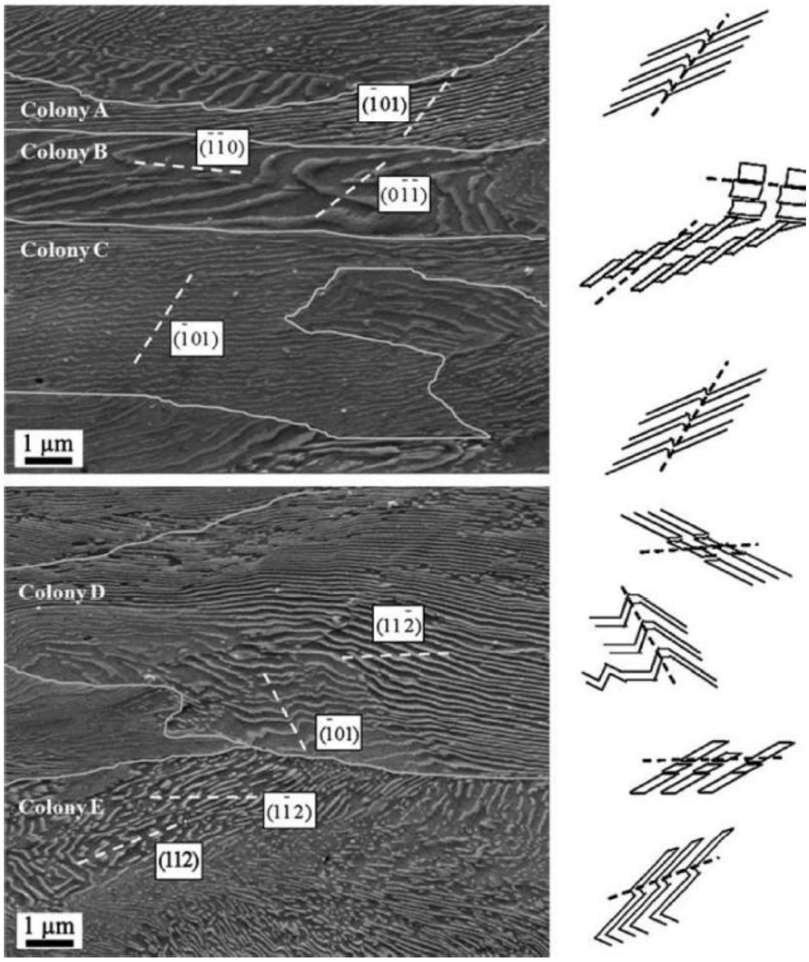

Figure 2.6: The traces of the {110} and {112} slip planes in ferrite [3].

2.2.5 Dynamic strain aging

Dissolution of cementite observed during wire drawing has been attributed to dragging of carbon atoms by the ferrite dislocations crossing cementite lamellae [1]. This leads to an oversaturation of ferrite by carbon atoms. The wire temperature increases during wire drawing (150-250 °C) and this oversaturation causes dynamic aging. Zelin [4] documented that dynamic aging results in higher ultimate tensile strength (UTS) but lower ductility (Figure 2.7).

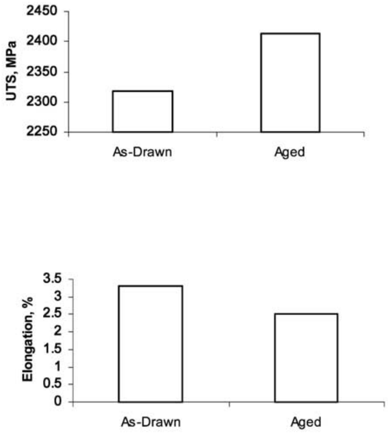

Figure 2.7: UTS and elongation to failure of an as drawn and an aged wire [4].

Dynamic aging has also an effect to increase the susceptibility to delamination. Figure 2.8 shows different fracture behaviour of a wire that is drawn with different speeds. It was observed that the wire that is produced with a low drawing speed does not deliminate under torsional loading (Figure 2.8 left side). The wire produced with higher drawing speeds delaminated under torsional loading (Figure 2.8 right side).

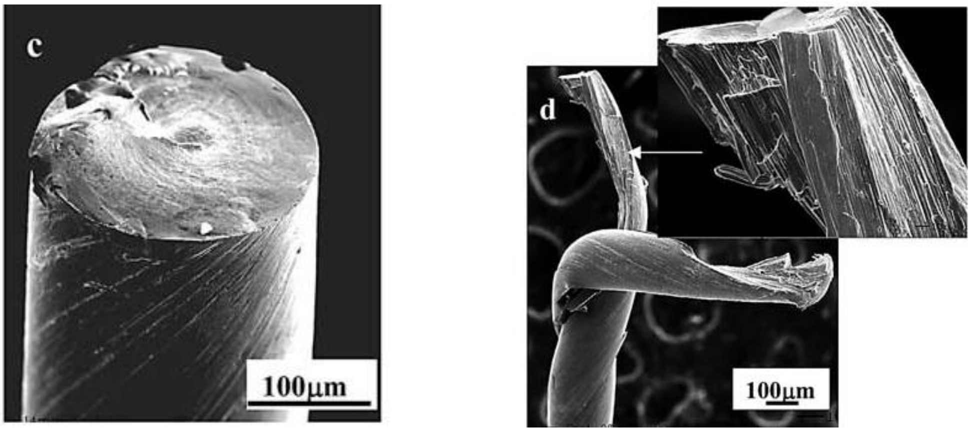

Figure 2.8: Delamination behaviors of a wire [8].

2.2.6 Residual stress development

Due to plastic deformation during the drawing process, a field of residual stresses and strains can remain in the cementite and ferrite phase. Neutron diffraction and X-ray methods are used to measure the amount of residual stresses.

The authors of more recent studies have proposed that the residual stresses may seriously influence both the mechanical properties and durability of the wires [12,13].

It is important to note that the diffraction peaks of cementite are very weak and difficult to clarify and the measuring of residual stress in pearlite eutectoid steels is difficult because the diffraction techniques obtain seperate values for the ferrite and cementite phases [1].

Van Acker et al. [12] investigated the residual stress state in the cementite as well as in the ferrite experimentally and obtained the measurements which are mainly based on neutron diffraction. They examined two drawn wires with a total strain of 1,96 and 2,59.

It was concluded in their study that the residual stress in the cementite is highly tensile, with values of 2000 MPa for the wire drawn to a strain of 1,96. The stress in the ferrite phase is compressive with values around -140 MPa. They also observed that the phase microstress is uniform through the wire cross section. They found that the stresses in the cementite phase of a wire drawn to a higher strain (2,56) are lower, about 1750 MPa.

Elice [13] examined pearlitic wires that are drawn to strain of 0,2 to understand the influence of residual stresses on some mechanical properties of the wires. He compared the drawn wires with wires that had a treatment to lower the residual stresses.

One wire was further drawn with a small area reduction (about 1%) and the another wire was heated to 400 °C and stretched under a tensile load of 0,4 σ_{max} at the same time.

Figure 2.9 shows a profile of computed longitudinal residual stresses, as a function of relative depth. Elice [13] concluded that the presence of residual stresses due to standard cold drawing (tensile stresses on the surface) favors the onset of yielding (Figure 2.10). It was observed that the higher residual stresses the lower is the yield stress in a tensile test.

Yang et al [14] investigated the residual stresses in the ferrite phase for different drawing strains up to 1,8 and used these results to calculate the macrostresses.

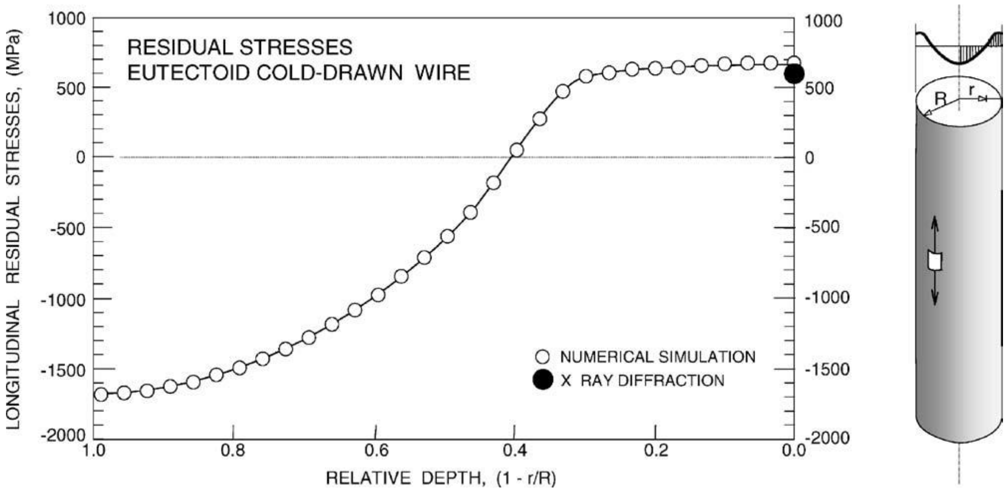

Figure 2.9: Longitudinal residual stresses in drawn steel wires [13].

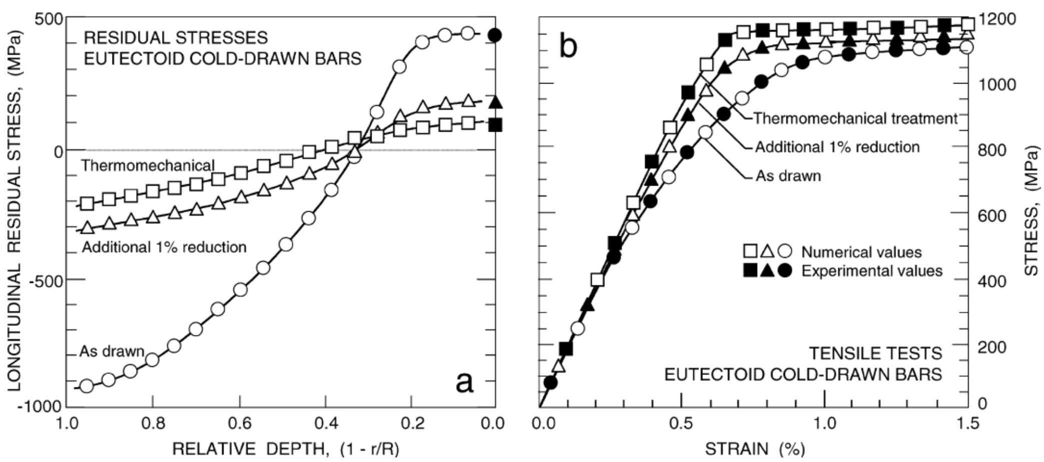

Figure 2.10: (a) Longitudinal residual stresses. (b) Stress-strain curves [13].

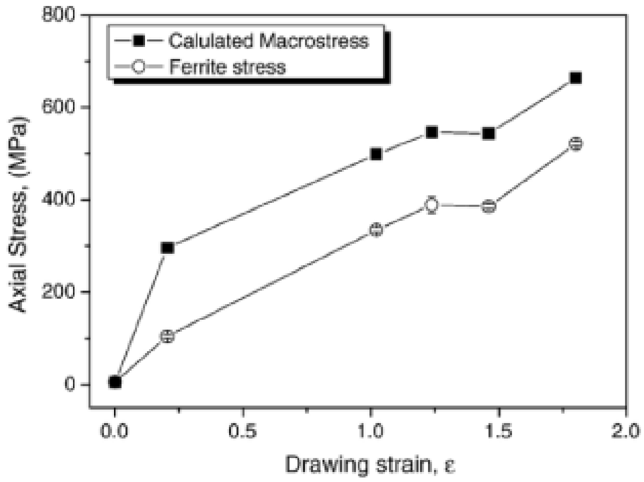

Figure 2.11: Axial stress as a function of drawing strain [14].

2.3 Tensile Test Properties of Heavily Drawn Steel Wires

2.3.1 Tensile test fractures of the heavily drawn steel wires

The ductility is very important for the heavily drawn steel wires, therefore it is expected to observe a ductile fracture surface after the wires were subjected to a tensile test.

The ideal tensile fracture is the classic cup-and-cone type which occurs in highly ductile materials (Figure 2.12). The classic cup-and-cone tensile fracture includes three zones: the inner flat fibrous zone where the fracture begins, an intermediate radial zone, and the outer shear lip zone where the fracture ends [15].

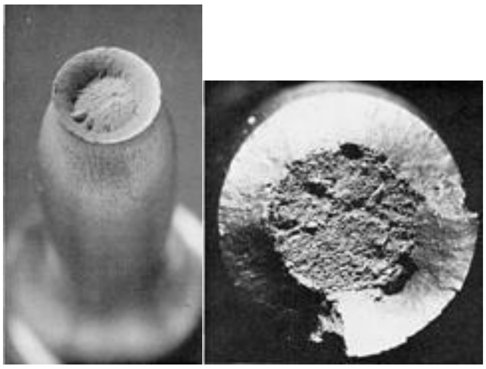

Figure 2.12: The classic cup-and-cone tensile fracture type. [21].

The fibrous zone is a region of slow crack growth at the fracture origin that is usually at or very close to the tensile axis. The radial zone results when the crack growth rate becomes rapid or unstable. The appearance of the radial marks is partly the result of the ductility of the material. The outer shear lip zone is a smooth, annular area adjacent to the free surface of the specimen [15].

2.3.2 Tensile test fracture behavior of the heavily drawn steel wires under mixed mode I+III

Davenport and Smith investigated the fracture behavior of notched solid round specimens under superimposed monotonic mode I and mode III loadings. The applied loadings were torque (mode III) and tensile load (mode I). The authors explain that plastic flow is relatively unconstrained in torsion and the plastic zone at the crack tip is large prior to fracture. Therefore, the subsequent tensile fracture toughness is considerably higher than that for mode I load alone [16].

It is the plastic flow at the crack tip that dictates the crack path. The notion that the crack path is governed by the plastic behaviour of the crack tip is supported by many workers. Under mode III loading ,the propensity for shear mode growth is strongly influenced by the plastic part of crack tip displacement [17].

In mode III, plastic zone is essentially circular and extends some four to six times further ahead of the crack than the symmetrical inclined shear distribution seen ahead of a pure mode I crack at the same stress intensity factor. The center of circular plastic zone lies somewhere between the tip of the crack and one radius distance ahead, depending on the work hardening coefficient [17].

Under mixed mode I+III, an increasing mode III contribution is known to lead to an increased concentration of the plastic strain in the trajectory of the crack as plastic zone changes from the twin lobed mode I to the circular mode III configuration, as shown in Figure 2.13 [17].

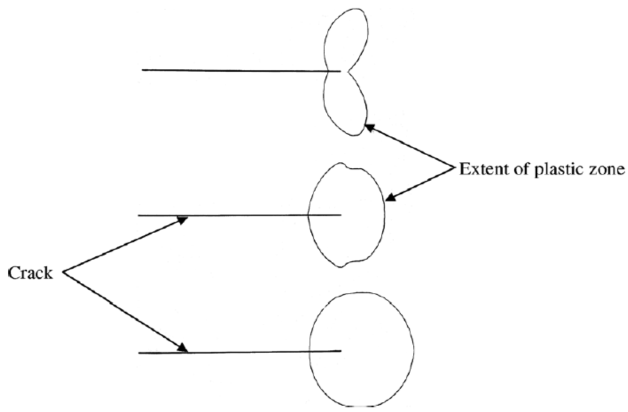

Figure 2.13: Plastic zone shapes: mode I (top), mixed mode I+III (bottom) [17].

2.4 Fatigue Properties of Heavily Drawn Steel Wires

This chapter describes the general fatigue properties of heavily drawn steel wires and the fatigue behaviors of various materail under mixed mode I+III.

2.4.1 Fatigue properties of heavily drawn steel wires under mode I

K. Lambrighs [1] investigated the fatigue properties of heavily drawn steel wires with a diameter of 175 μm which were produced by NV Bekaert SA. Pull-pull fatigue tests were performed at a frequency of 60 Hz and with a gauge length of 80 mm.

K. Lambrighs [1] first studied the fatigue life at one stress level (σ_a=707 MPa) (Figure 2.14).

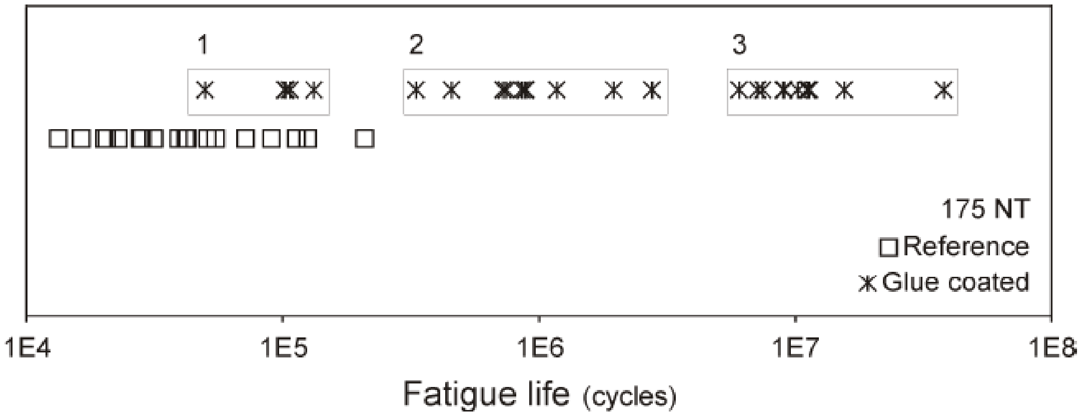

Figure 2.14: Fatigue data of reference and glue coated wires [1].

From the figure 2.14 the data points of glue coated wires can be subdivided into three groups, indicated as 1,2 and 3. There are three different fatigue crack inititaion mechanisms active. A surface stress concentration mechanism is active for both group 1 and group 2, the internal stress concentration mechanism is active for group 3.

K. Lambrighs [1] observed two different fatigue mechanisms which are active for heavily drawn steel wires, namely surface crack inititaions and internal crack inititaions (Figure 2.15).

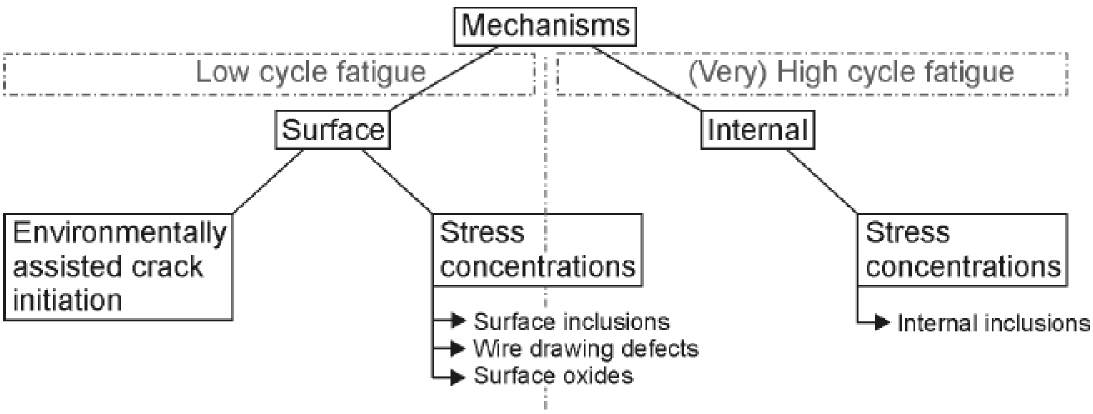

Figure 2.15: Overview of fatigue crack inititation mechanisms [1].

He observed that the fatigue cracks grow semi circular or semi elliptical when the fatigue crack initiates from surface and circular or elliptical when the fatigue crack inititates internally (Figure 2.16). The white arrows show the residual fracture towards the fatigue crack inititaion area. The internal fatigue crack inititaion area is indicated with a white ellipse.

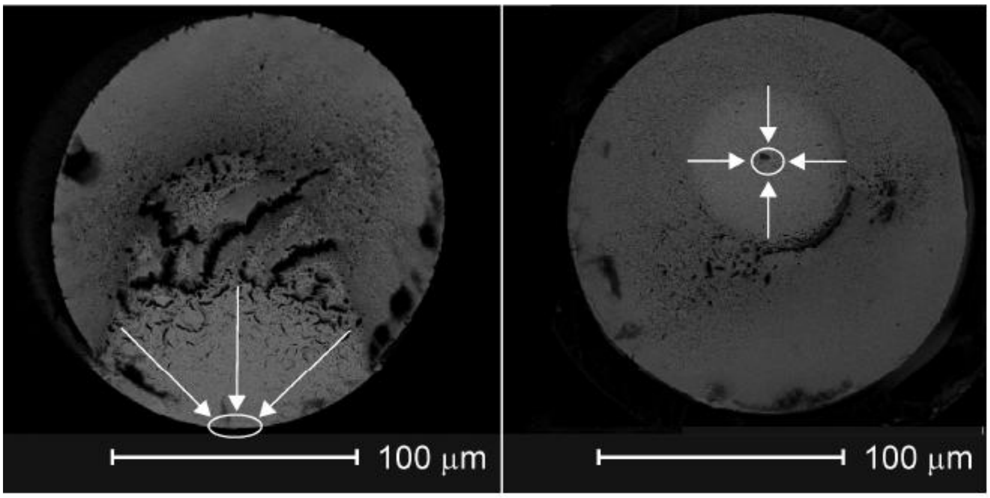

Figure 2.16: Fatigue crack areas (a) Surface. (b) Internal [1].

In according to Murakami's formulae [18] for fatigue cracks, the stress intensity factor range due to the difference in boundary conditions between internal and surface fatigue cracks.

$$\Delta K_{surface}=0.65\ \Delta\sigma\ \sqrt{\pi\sqrt{area}} \quad \textbf{(2.2)}$$

$$\Delta K_{internal}=0.5\ \Delta\sigma\ \sqrt{\pi\sqrt{area}} \quad \textbf{(2.3)}$$

where ΔK the stress intensity factor range [MPa$\sqrt{m}$], Δσ the applied stress range [MPa], $\sqrt{area}$ the root of the area of fatigue crack.

2.4.1.1 Surface crack inititaion mechanism

The surface crack inititaion mechanism can be divided into two groups; environmentally assisted crack inititaion and the crack initiation at the surface stress concentrations. Both of these mechanisms can be active at the same time. K. Lambrighs [1] observed that the surface crack initiation mechanisms mostly lead to low cycle fatigue lives (LCF), therefore they determine the fatigue properties of the steel wire.

- **Enviromentally assisted crack inititaion**

Because enviromentally assisted crack initiation mechanism leads to low cycle fatigue lives, it is a dominant mechanism and determines the fatigue properties of

steel wires. It is important to note that only surface fatigue cracks are effected by enviromental interactions.
It is well known that the presence of corrosion products with clorides at the surface of the wire decreases the fatigue lives of heavily drawn steel wires significantly (Figure 2.17). K.Lambrighs [1] observed that the removal of the surface clorides by cleaning operation improves the fatigue lives but when the clorides are captured inside corrosion spots and if the environmentally assisted mechanism is not active, the cleaning operation does not work.

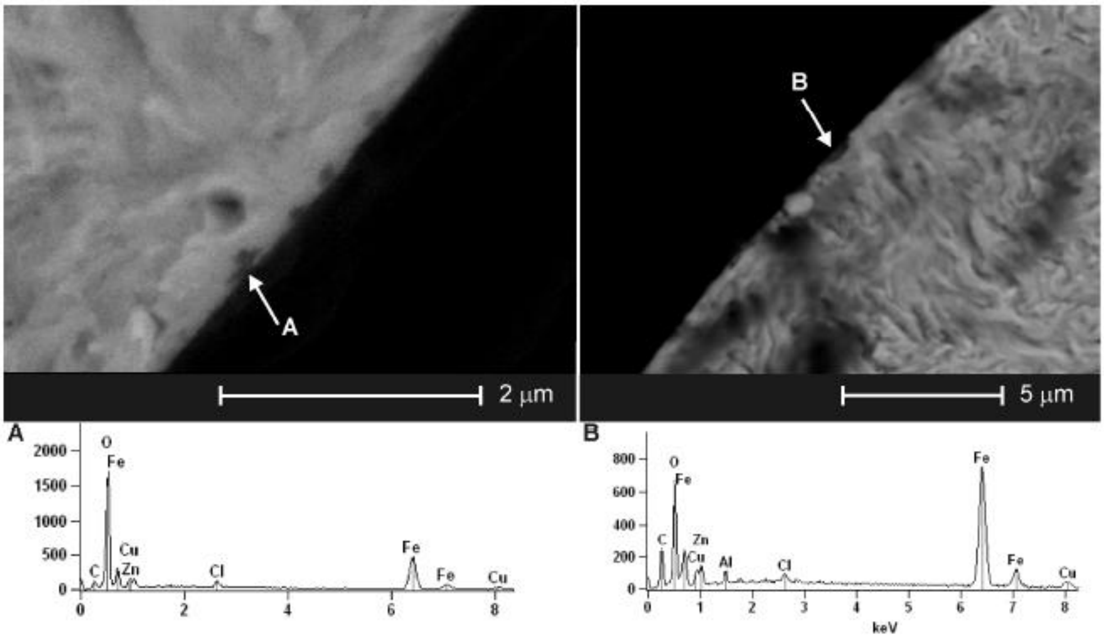

Figure 2.17: The presence of corrosion products with clorides at fracture area [1].

K.Lambrighs investigated the influence on the fatigue life by coating the wires and he performed the fatigue tests at three different stress levels (σ_a=416, 520 and 624 MPa) and an R value of 0.5. Two different coatings are used, namely a Sicomet 50 cyano-acrylate glue coating and benzotrialzole coating. It is important to clean the wires by wiping the surface at least 5 times with acetone to remove the dirt and residual lubricant, followed by wiping the surface at least 2 times with ethanol to remove the residual acetone. The glue reacts with the water that is present at the surface of the wire. Both of the cleaning operation before the coating and the reaction between the glue and the water (corrosion is impossible without water) improves the fatigue lives of the steel wire (Figure 2.18).

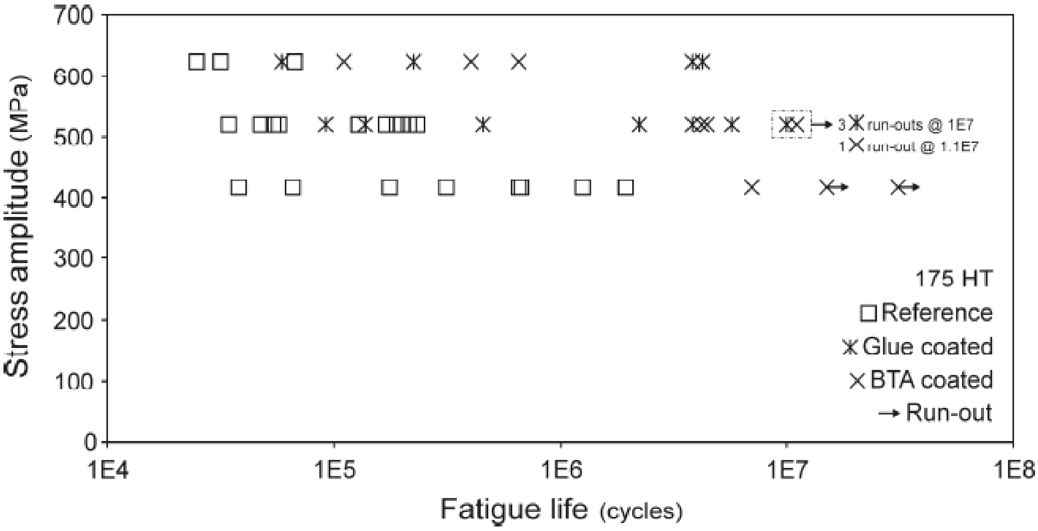

Figure 2.18: Fatigue data of coated and reference wires [1].

❖ **Crack inititaion at surface concentrations**

☞ **Group 1**

The initial stress intensity factor ΔK of surface stress concentration determines the fatigue life of the metal. When ΔK is larger than ΔK_{th} (threshold value of crack growth) the long fatigue cracks can immediately start growing which means the low fatigue lives are observed. K.Lambrighs concluded that the fatigue life of the steel wire depends on only the size of the defect , not the kind of surface stress concentration.

It was observed that the long fatigue cracks grow in a plane perpendicular to the applied load (Figure 2.19).

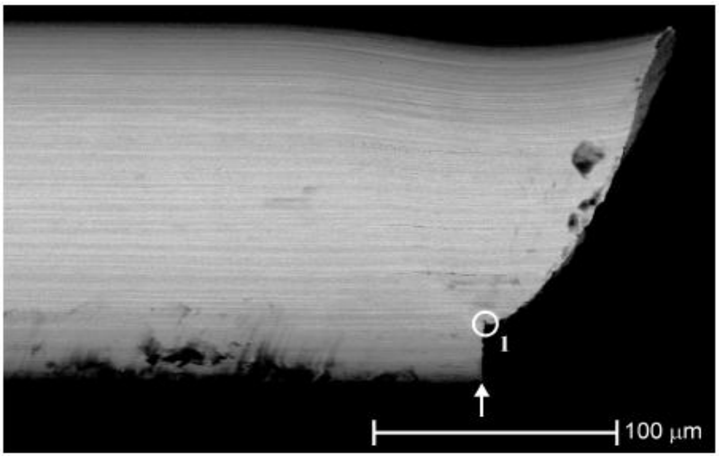

Figure 2.19: Growth of the long fatigue cracks perpendicular the wire axis [1].

The fracture plane of a typical surface crack inititaion can be seen in the figure 2.20. The white arrow indicates the fatigue inititaion area and the dotted white line indicates the end of the fatigue fracture.

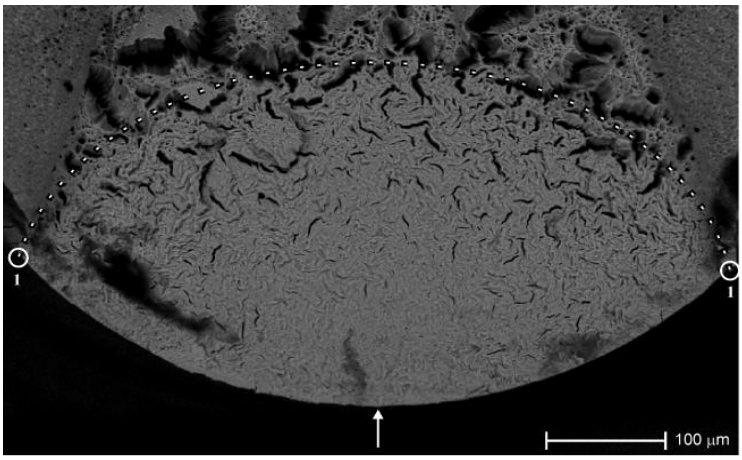

Figure 2.20: Fracture plane of a surface crack inititaion [1].

K.Lambrighs observed secondary cracks which have a wavy shape on the fracture plane and these secondary cracks follow the wire axis and are formed during the crack growth to relieve existing stresses at crack tip. Due to stress relief, deep secondary cracks are followed by shallow ones (Figure 2.21A). After this formation of the secondary cracks, the fatigue crack continues to grow on the place where the resistance against crack growth is locally at a minimum and this leads to a fatigue fracture plane that is not flat, but jumps up and down at secondary cracks (Figure 2.21B).

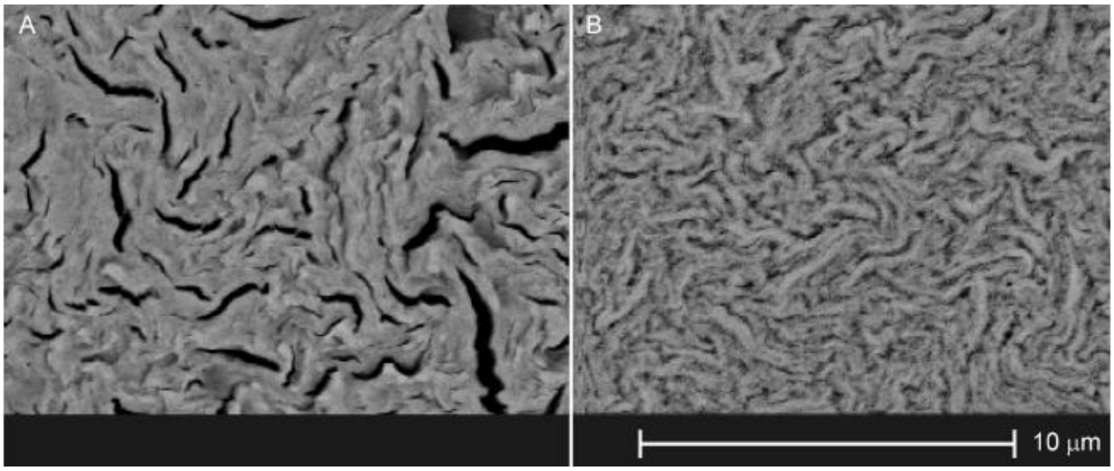

Figure 2.21: (a) Fracture surface. (b) Microstructure of the cross section [1].

It is possible to predict to total fatigue life by using Paris law for long fatigue cracks [19]. The Paris formula is shown in equation **(2.4)**.

$$\frac{da}{dN} = C\Delta K^m \quad \textbf{(2.4)}$$

where $\frac{da}{dN}$ is a crack growth speed and C and m are material parameters.

☞ **Group 2**

It was observed that when $\Delta K < \Delta K_{th,}$ fatigue cracks occurs at low crack growth rates. In this group two kind of fatigue cracks are observed, namely SiO_2 inclusion and a surface defect. Figure 2.22A shows this surface defect which follows the wire axis and figure 2.22B shows that a subsurface SiO_2 inclusion located at crack inititaion area. The facet area was observed when the short cracks initiated internally, but when the short cracks initiated from the surface no characteristic area is formed.

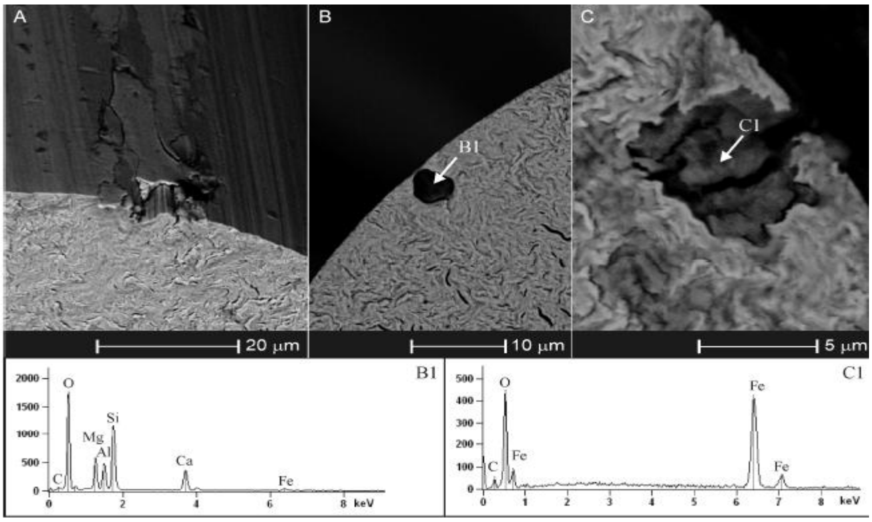

Figure 2.22: (a) Surface defects. (b) Surface inclusion. (c) Surface oxides [1].

2.4.1.2 Internal crack inititaion mechanism

The fatigue crack initiated internally for this fracture mode and the size of internal defect determines the fatigue life of the steel wire.

☞ **Group 3**

Short fatigue cracks initiates at internal inclusions of the material and this fracture mode leads to very high cycle fatigue lives (VHCF) when $\Delta K < \Delta K_{th.}$ The fracture surface can be seen in Figure 2.23. As can be seen from the figure the roughness area around the inclusion is significantly higher than the normal fracture surface. This rough area around the internal inclusions is only observed for the internal crack growth when $\Delta K < \Delta K_{th}$. The region of short crack growth around the inclusion is called as optical dark area (ODA), the facet area (FCT), granular bright facet (GFA) or fine granular area (FGA).

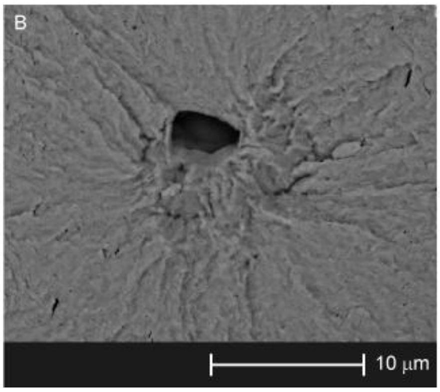

Figure 2.23: Internal fatigue crack initiation for $\Delta K<\Delta K_{th}$ (B) [1].

K.Lambrighs [1] obtained the fatigue data of the different fatigue crack inititation mechanisms presented in SN graph (Figure 2.24). It can be concluded that high cycle fatigue behaviour is observed when surface concentrations with $\Delta K< \Delta K_{th}$ and internal stress concentrations with $\Delta K< \Delta K_{th}$ leads to very high cycle fatigue lives.

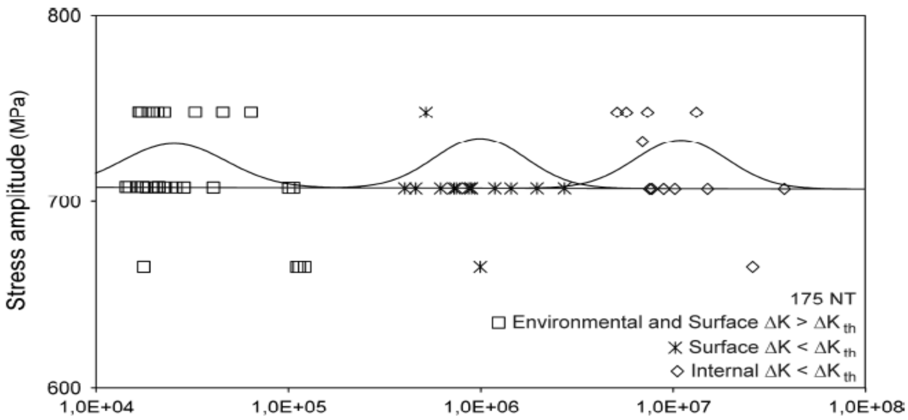

Figure 2.24: Fatigue data of the different fatigue crack inititation mechanisms [1].

2.4.2 Fatigue properties of various materials under mixed mode I+III

Although the majority of the fracture mechanics data and analyses are investigated for mode I loading, the structures are subjected to combinations of cyclic loads acting in different directions and many service failures occur from cracks subjected to mixed mode loadings.

Hourlier and Pineau [20] conducted static mode III and cyclic mode I tests using notched specimen made of two titanium and two steels. They observed that the addition of static mode III load causes a strong decrease (as much as two orders of magnitude) in fatigue crack growth rate, as compared to pure mode I behavior. After they measured the load line displacement as a function of the axial load, it was concluded that a strong mode I crack closure effect leads a reduction of crack growth rate, due to the applied static mode III [16].

Tschegg et al.[21] investigated crack face interactions using solid round specimen with notches between mode I and III loads. They observed that the fatigue crack growth rates reduced with an increase of mode III static load and the ΔK_{th} values increased steadily with increasing the static mode III.

M.Fonte et al. [22] investigated the effect of steady torsion on fatigue crack growth in shafts. They used DIN Ck45k for their study and observed a significant reduction of the crack growth rates when a steady torsion mode III is superimposed to cyclic mode I. The fatigue crack growth (FCG) for rotary bending and rotary bending combined with steady torsion mode I are shown in figure 2.25. The figure 2.25 reveals that FCG rate in rotary bending decreases with the level of steady torsion.

Figure 2.26 shows the evolution of the arc crack length for a specimen with a diameter of 14 mm under alternating bending combined with steady torsion. As can be seen from the figure 2.26 the torsion level causes a signifacnt effect on the reduction of FCG rate and on the fatigue crack front profile rotation. They also observed that the lifetime between the crack inititaion and the final fracture is longer than for pure mode I when the steady torsion load mode III is superimposed to mode I.

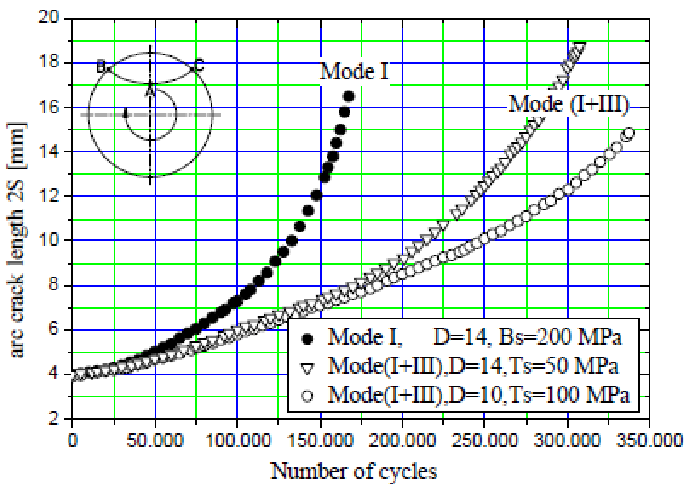

Figure 2.25: Crack length as a function of number of cycles in rotary bending [22].

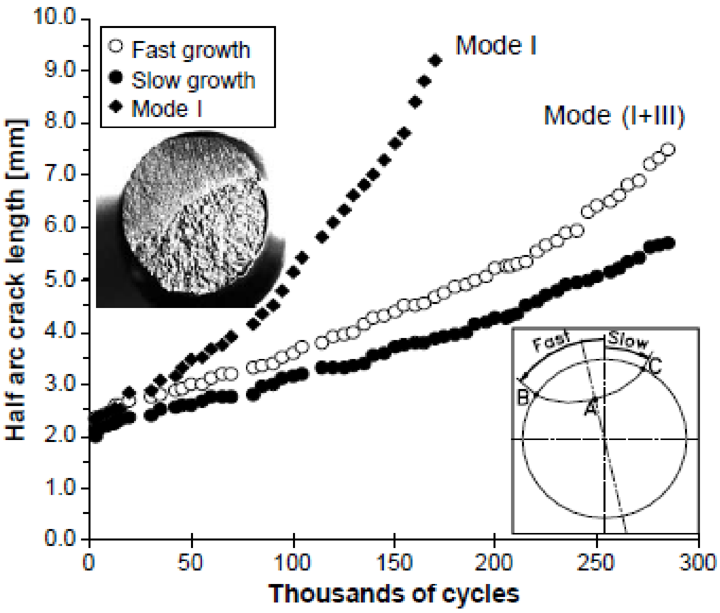

Figure 2.26: Crack growth curves in bending combined with torsion [22].

SEM results of M.Fonte et al [22] revealed a zig-zag crack path on the cylindrical surface of the specimens and also on the crack surface, due to torsion, which is a significant safety factor that decreases the FCG rate. In figure 2.27, the SEM fatigue crack growth morphology shows a factory roof which explains the zig-zag crack path and the effect of friction between crack surfaces due to torsion.

The authors of more recent studies have proposed that a significant decrease in mode I fatigue crack growth rate can result from the contribution of a static mode III load. The presence of a static mode III load causes a strong mode I crack closure effect.

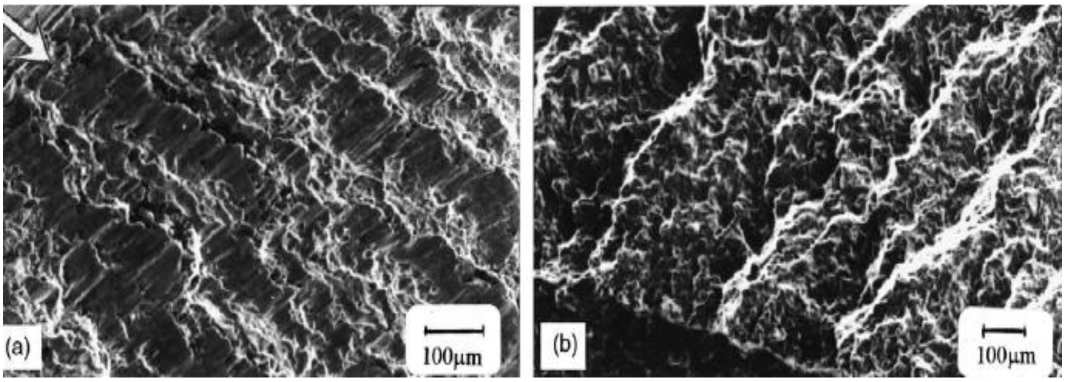

Figure 2.27: Factory roof: (a) near the notch. (b) closed to the crack tip [22].

3. EXPERIMENTAL STUDIES

3.1 Materials and Methods

Tensile tests and hardness tests are performed to determine the influence of torsion on the static properties of steel wires. The fatigue tests are performed to determine the fatigue properties of heavily drawn steel wires under mode I and mode I+III.

All the tests in this project are performed on brass coated steel wires with a diameter of 175 μm.

3.2 Sample Preparation

The same sample preparation is used for all the tests. The heavily drawn steel wires are stored in a dessiccator to prevent any corrosion. The samples used in this study have a gauge length of typically ≅50 mm as shown in Figure 3.1. The cleaning operation is done to remove dirt and residual lubricant. The samples are cleaned by wiping the surface with acetone at least 5 times to remove surface contaminants, followed by wiping the surface with ethanol at least 2 times to remove the residual acetone. The ends of the wire are glued between two aluminium plates. The plates should not have any sharp edges to avoid any mechanical damage to the samples. The ends of the wire are bent around the plates to improve fixation of the wire during the tension test. After these operations, the samples is coated by a Sicomet 50 cyano-acrylate glue coating.

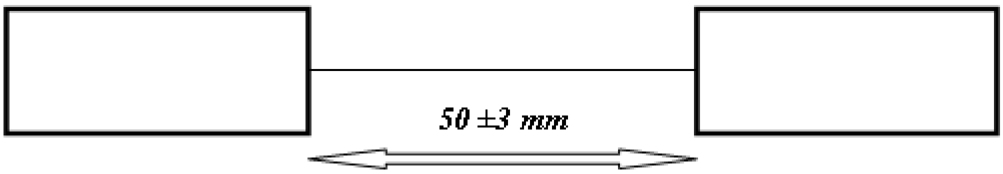

Figure 3.1: The gauge length should be uniform for each sample, ≅50±3 mm.

3.3 Tensile Tests

The tensile tests were perfomed to investigate the static behaviour of steel wires under superimposed monotonic mode I and mode I+III. The loading sequence consists of torsion first followed by tension. Prior to testing the gauge length, L_0, was measured. A strain rate of 0,5 mm/min was used. For each set of tests, the average result was calculated and average test curves are shown on the graphs.

To determine the effect of torsion on the tensile properties of the sample, different amount of torsion was applied, respectively. Twisting was performed by hand using the device shown in Figure 3.2.

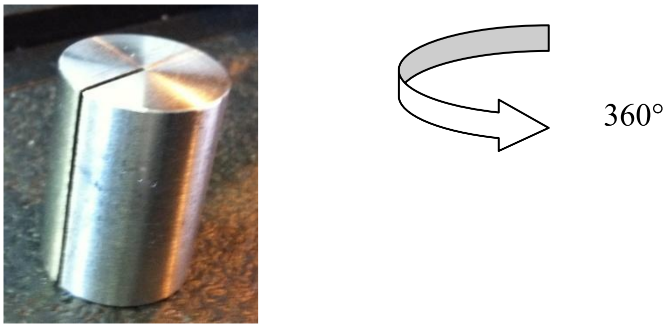

Figure 3.2: The device for twisting the wire before mounting it in machine.

Table 3.1: The sample identification used in the following sections of this report.

			Test Schedules			Representation
I.	**Twisting**	⇨	**Tensile Test**			[a]
II.	**Twisting**	⇨	**Sample released**	⇨	**Tensile Test**	[b]

In order to understand the effect of torsion on the tensile properties of the sample, the tests were carried out in two different ways as indicated above (Table 3.1).

Type of method and number of rotations are shown in Figure 3.3 for tensile tests.

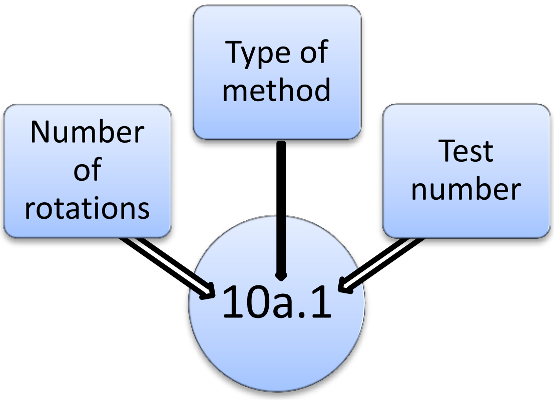

Figure 3.3: Representation of the sample idendification scheme.

3.3.1 Tensile test results and comparisons

Properties obtained from the tensile tests include; maximum tensile load (P), modulus of elasticity (E), engineering stress (S), engineering strain (%e), true stress (σ) and percent true strain (%ε). Load and extension were recorded during the test. A load-extension graph is converted into an engineering stress-strain graph by using the following equations;

$$S=\frac{P}{A_0} \quad \textbf{(3.1)}$$

$$e=\frac{\delta}{L_0}=\frac{\Delta L}{L_0}=\frac{L-L_0}{L_0} \quad \textbf{(3.2)}$$

where;

P: Load (N)

A_0: Cross section area (mm^2)

S: Engineering stress (MPa)

e: Engineering strain

L_0: Gauge length of specimen (mm)

L: The length of the specimen after the test (mm)

The cross section was calculated from the following equation;

$$A_0=\frac{\pi\times D_0^2}{4} \quad \textbf{(3.3)}$$

D_0= Diameter of the specimen (mm)

From the engineering stress-strain, the true stress-strain relation was calculated using the constant volume assumption which results in the following relationships;

$$\sigma= S(e+1) \quad \textbf{(3.4)}$$

$$\varepsilon=\ln(e+1) \quad \textbf{(3.5)}$$

where;

σ: True stress (MPa)

ε: True strain

The tensile test values for each test were calculated using these equations and denoted in tables. All the tensile test results and graphs can be found in the Appendix A.

The average values obtained from the tests are indicated respectively in Table 3.2 and Table 3.3 for the two test schedules and 0 rotation.

The tensile test curves which are obtained based on the average results of tests are shown in Figure 3.4 and Figure 3.5.

Figure 3.6 shows the changes in maximum tensile load with increasing number of rotations, Figure 3.7 shows the changes in total true strain with increasing number of rotations and the changes in maximum true stress with increasing the number of rotations are shown in Figure 3.8.

Table 3.2: Overview of average tensile test results for 'type a (rotation+tensile)'.

Test Number	Rotations	Test Rate, r (mm/min)	Diameter, D_0 (mm)	Max. Tensile Load, P (N)	Modulus of Elasticity, E (GPa)	Engineering Stress, S (MPa)	Max. Engineering Strain, e (%)	True Stress, σ (MPa)	True Strain, ε (%)
0(a)	0	0,5	*0,175*	*75,29±1,36*	*168±7,5*	*3136±57,2*	*2,48±0,12*	*3209±61,8*	*2,33 ±0,12*
10(a)	10	0,5	*0,175*	*69,57±3*	*161±8,7*	*2810,25±80*	*2,74±0,6*	*2885±85*	*2,72±0,6*
20(a)	20	0,5	*0,175*	*71,03±0,96*	*157±10*	*2953±40*	*3,62±0,25*	*3059±42*	*3,61±0,25*
30(a)	30	0,5	*0,175*	*70,05±1,5*	*160,2±5,5*	*2890,3±55,12*	*3,49±0,26*	*2989,8±59*	*3,43±0,26*
40(a)	40	0,5	*0,175*	*68,6±0,29*	*164±8,8*	*2859,8±12*	*3,94±0,13*	*2976±14*	*3,86±0,13*
50(a)	50	0,5	0,175	67,29±1,49	169±15	2684±55	3,41±0,3	2781±65	3,36±0,3

Table 3.3: Overview of average tensile test results for '(rotation+release+tensile)'.

Test Number	Rotations	Test Rate, r (mm/min)	Diameter, D_0 (mm)	Max. Tensile Load, P (N)	Modulus of Elasticity, E (GPa)	Engineering Stress, S (MPa)	Max. Engineering Strain, e (%)	True Stress, σ (MPa)	True Strain, ε (%)
10(b)	10	0,5	*0,175*	*70,94±3,16*	*163,5±3,2*	*2955,67±127*	*2,70±0,3*	*3033,3±128*	*2,66±0,3*
20(b)	20	0,5	*0,175*	*71,03±0,28*	*157±3*	*2986,2±15*	*3,23±0,2*	*3090±32*	*3,18±0,2*
30(b)	30	0,5	*0,175*	*70,7±0,3*	*161,2±3*	*2942,3±11*	*3,27±0,14*	*3037,3±16*	*3,22±0,14*
40(b)	40	0,5	*0,175*	*67,3±2,46*	*163±6,8*	*2802±102*	*3,19±0,55*	*2890,8±120*	*3,13±0,53*
50(b)	50	0,5	*0,175*	*68,82±0,2*	*160±3,3*	*2883±163*	*3,32±0,77*	*2978±189*	*3,27±0,74*

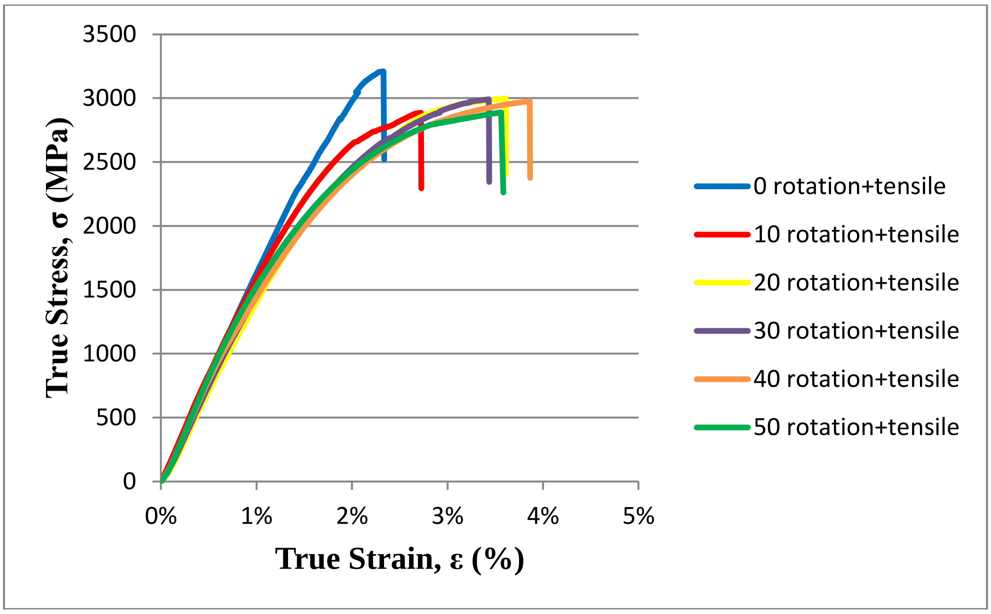

Figure 3.4: True stress as a function of true strain for 0 rotation and type (a).

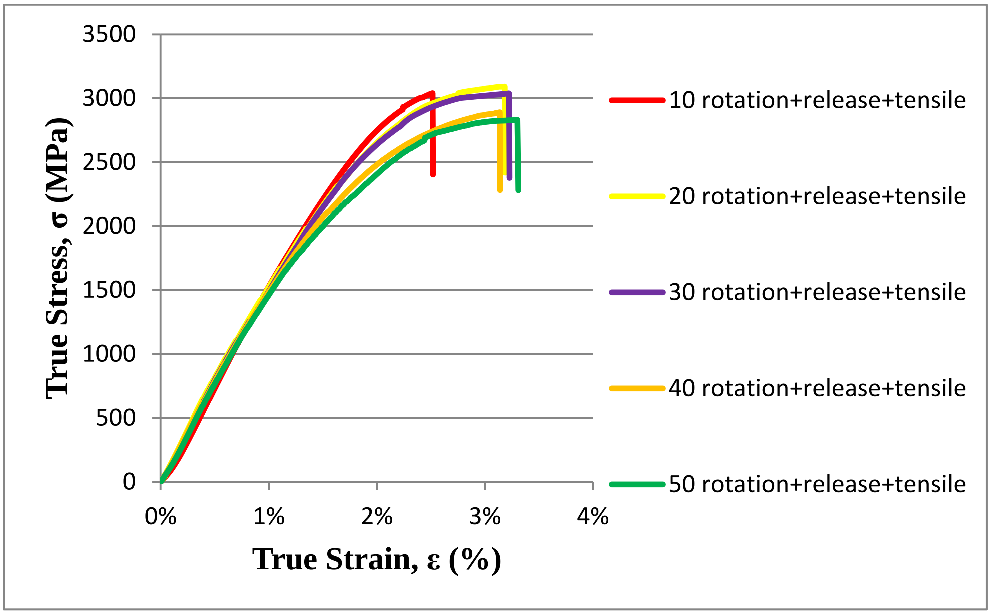

Figure 3.5: True stress as a function of true strain for type (b).

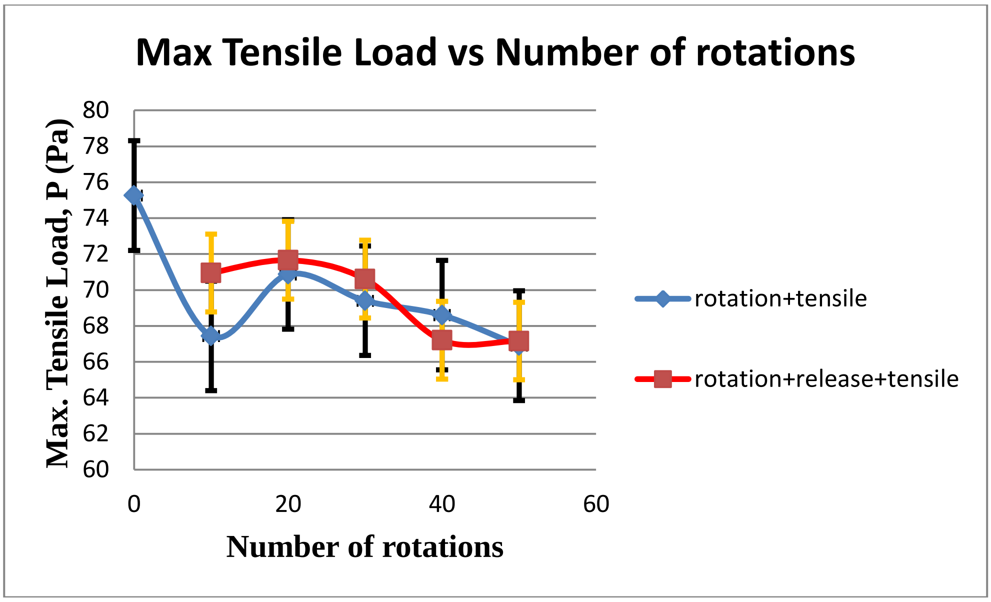

Figure 3.6: Maximum tensile as a function of the number of rotations.

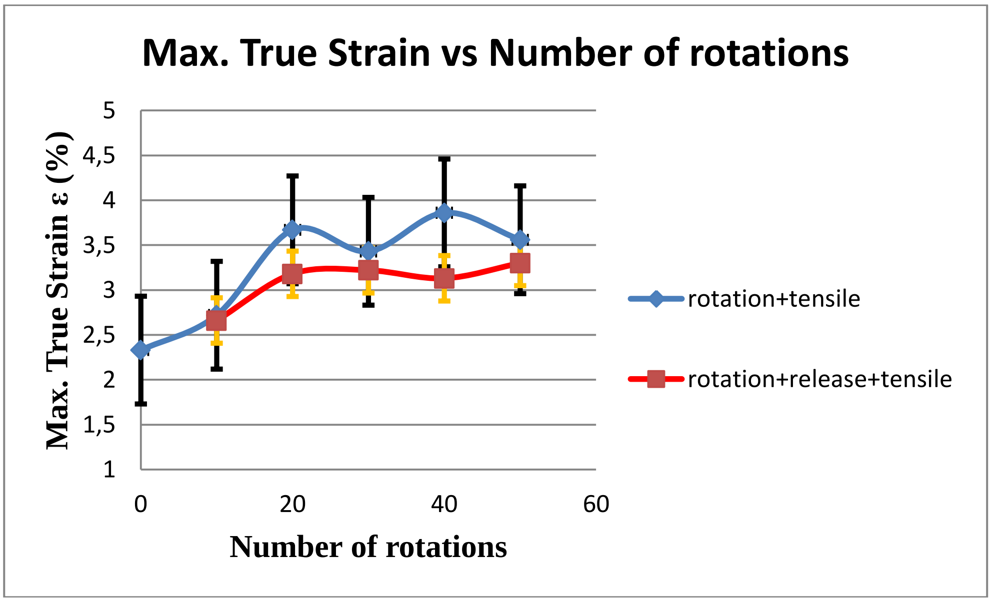

Figure 3.7: Maximum true strain as a function of the number of rotations.

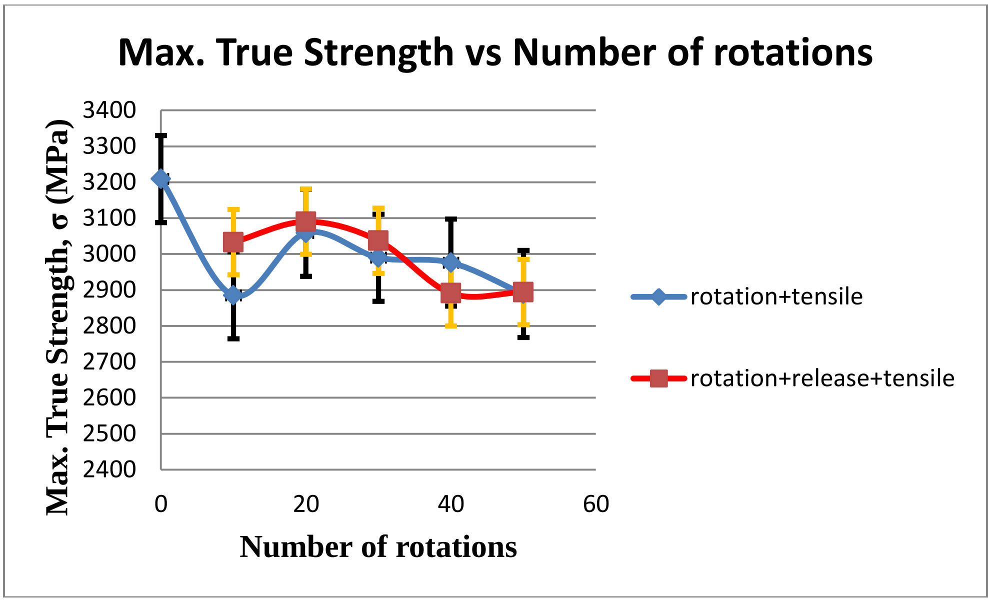

Figure 3.8: Maximum true stress as a function the number of rotations.

3.3.2 Fractography

After the tensile test, the fractured samples are positioned vertically in the vacuum chamber of the scanning electron microscope (SEM) to analyse the fracture surface of the heavily drawn steel wires.

Cup-and-cone tensile fracture and dimples which are asscociated with ductile materials were observed on the fracture surface of the samples (Figure 3.9). The classic cup-and-cone tensile fracture includes three zones: the inner flat fibrous zone where the fracture begins, an intermediate radial zone, and the outer shear lip zone where the fracture ends [21].

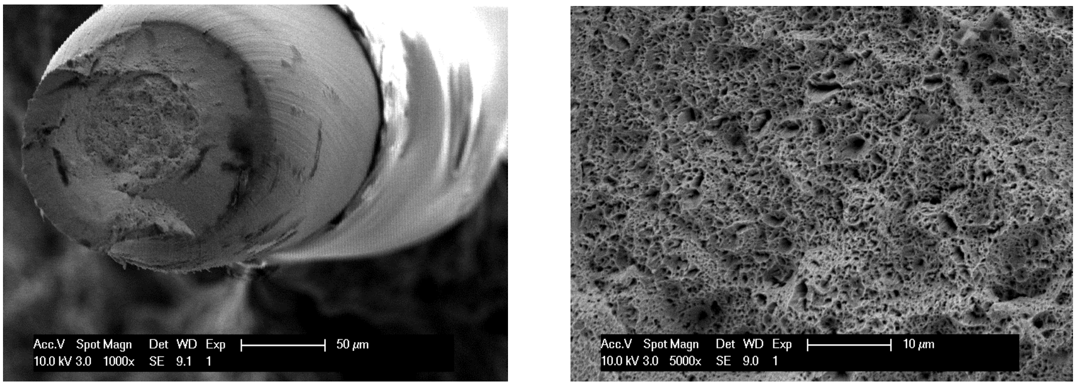

Figure 3.9: SEM images: (a) Cup-and-cone tensile fracture. (b) Dimples.

3.3.3 Conclusions

The influence of torsion on static properties of steel wires was investigated in this study. Based on the tensile test results one can conclude that increasing numbers of rotations result in lower strength and higher ductiliy.

It is important to note that decrease in the strength and increase in the ductility is not proportional to the torsion.

The authors of more recent studies proposed that the plastic flow is relatively unconstrained in torsion and creating the large plastic zone at the crack tip prior to fracture. The contribution of mode III leads to change the plastic zone shape from the twin lobe mode I to the circular mode III configuration. Therefore, the subsequent tensile fracture toughness is considerably higher than that for mode mode I load alone.

It is important to emphasize that the strength of high carbon steel wire is not homogenous, due to inhomogenous cementite decomposition during drawing. Therefore, the torsional deformation does not propagate easily in a steel wire and tends to accumulate locally. As a consequence, the torsional deformation concentrates where cementite decomposed less, where strength is lower and leading to crack.

3.4 Hardness Tests

The vickers micro hardness test method was performed to determine the hardness properties of steel wires under mode I and mode III. 50 gr load cell was used for the hardness tests.

3.4.1 The hardness test results and comparisons

The average micro hardness values are obtained on the center, close to surface and closest to surface of the steel wire and indicated in Table 3.4. All the hardness test results for different amount of torsion can be found in Appendix B.

Table 3.4: The average vickers micro hardness values of steel wire.

Torsion	Closest to surface (Average HV)	Close to surface (Average HV)	Center (Average HV)
0	724,5	724,6	790,9
10	682,2	703,8	712,1
20	655,6	655,1	702,9
30	696,7	742,1	740,3
40	709,3	726,6	740,3
50	725,5	711,8	695,9

From the figures (Figure 3.10, 3.11 and 3.12) it is apparent that the changes in hardness values are not proportional to the number of rotations. The results of the present study demonstrate that the hardness values decrease up to the number of 20 rotations on the cross section.

It is important to note that after the number of 20 rotations, the hardness values increase with increasing rotations on the surface. The hardness values that are obtained towards to the center of cross section reaching the highest value at 30 rotation and decreasing for 40 and 50 rotations.

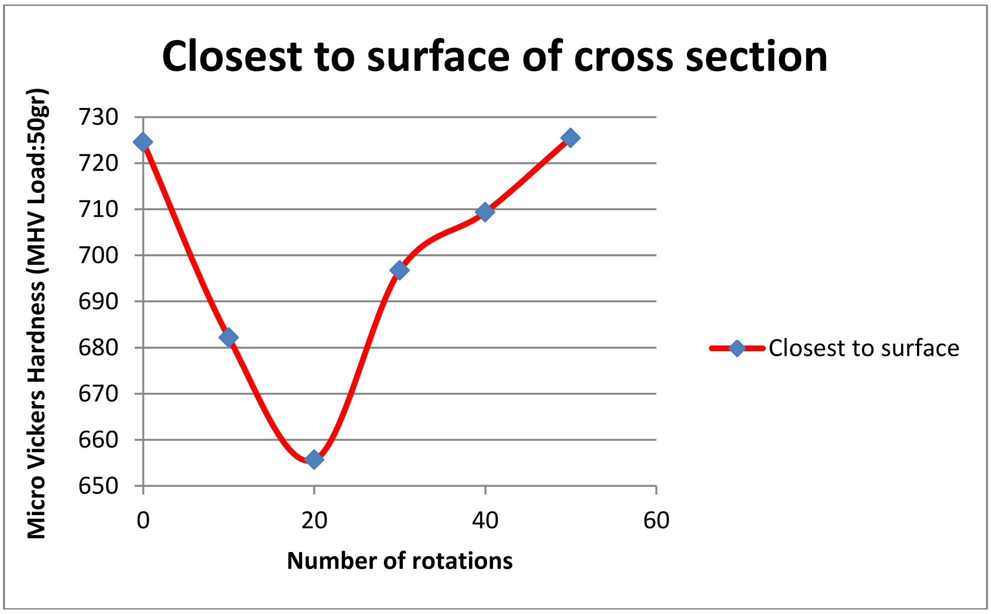

Figure 3.10: Micro hardness values on the closest to surface of cross section.

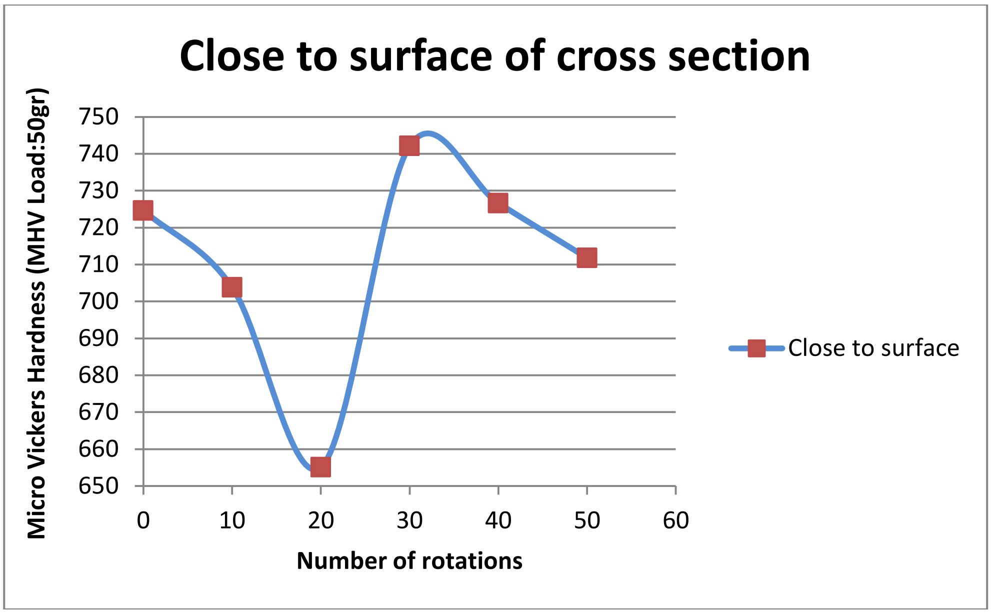

Figure 3.11: Micro hardness values on the close to surface of cross section.

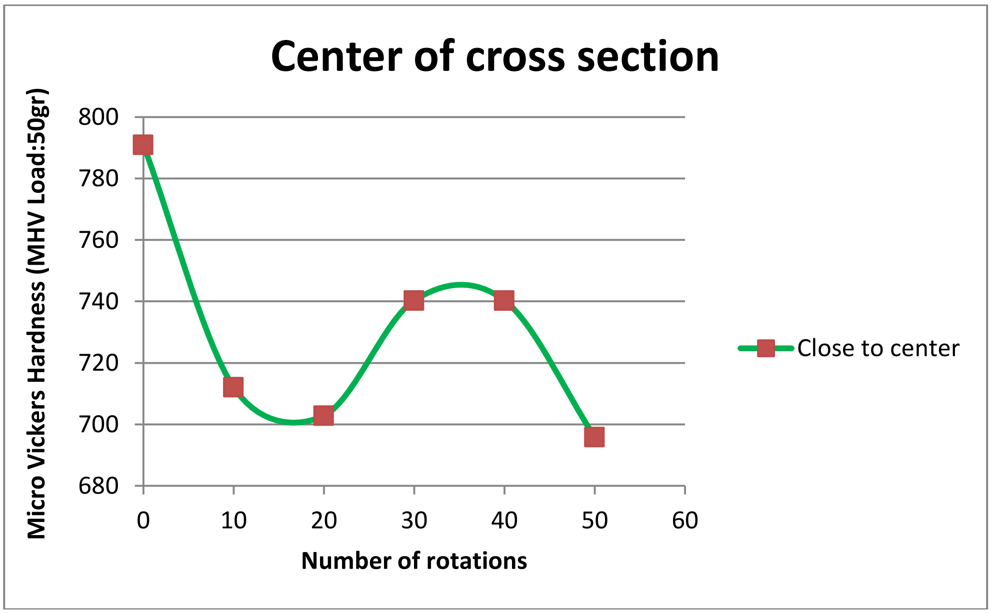

Figure 3.12: Micro hardness values on the center of cross section.

3.4.2 Conclusions

According to the experimental results of hardness tests, it can be seen that the hardness of the steel wire is not homogenous. Due to inhomogenous cementite decomposition during drawing, the torsional deformation does not propogate easily in a steel wire and tends to accumulate locally. Therefore, all of this points to the fact that the hardness values are not proportional with the torsional deformation and when the sample subjected to twisting 20 times, the lowest hardness values are observed.

3.5 Fatigue Tests

Pull-pull fatigue tests were performed at a frequency of 50 Hz and with a gauge length of 50 mm. An Instron E3000 Electropuls fatigue machine was used for the fatigue tests. Samples were prepared as described in paragraph 3.2. All the fatigue tests were performed on the 175 µm heavily drawn steel wires at a R value of 0.5.

3.5.1 Fatigue test results and comparisons

In order to determine the influence of the torsion the samples were fatigue tested at 6 different number of rotations (0-2-10-20-30-40-50) (Table 3.5). Only one stress amplitude was chosen for the fatigue tests, σ_a= 676 MPa. The fatigue test results for 0, 2 and 10 rotations are given in the following figures (Figure 3.13,3.14 and 3.15). Two different fracture mechanisms, namely surface and internal fatigue crack inititaions, are active in sample with 0 and 2 twists. No internal cracks were observed in sample with more than 2 twists. Figure 3.16 describes stress amplitude as a function of fatigue life for different amount of torsion. All the fatigue test results are given in Appendix C.

Table 3.5: Overview of loading conditions and amount of repetitions..

Number of rotations	R	σa (MPa)	σ_{mean} (MPa)	σ_{max} (MPa)	σ_{min} (MPa)	#samples
0	0.5	676	2027	2702	1351	14
2	0.5	676	2027	2702	1351	20
10	0.5	676	2027	2702	1351	6
20	0.5	676	2027	2702	1351	3
30	0.5	676	2027	2702	1351	4
40	0.5	676	2027	2702	1351	4
50	0.5	676	2027	2702	1351	5

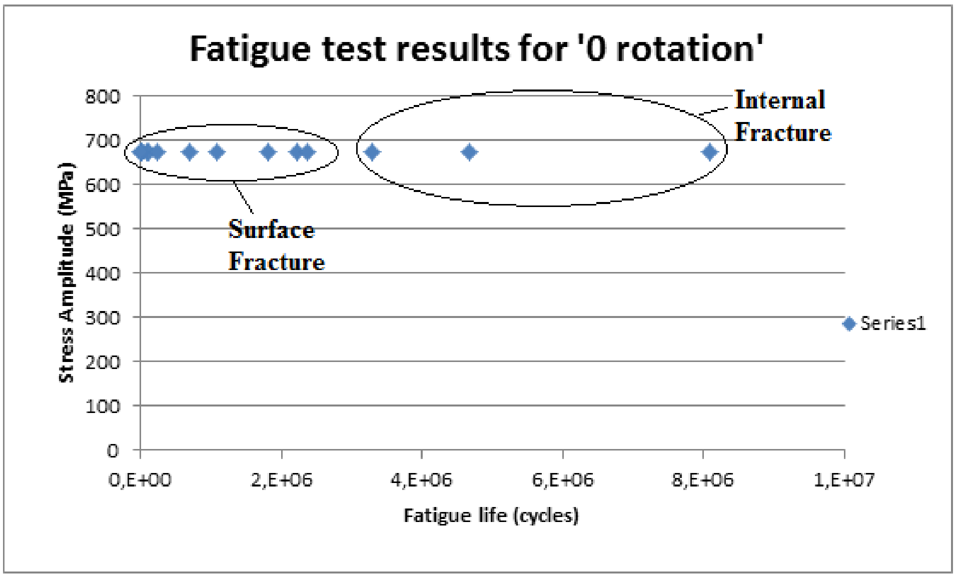

Figure 3.13: Stress amplitude as a function of fatigue life for ‘0 rotation’.

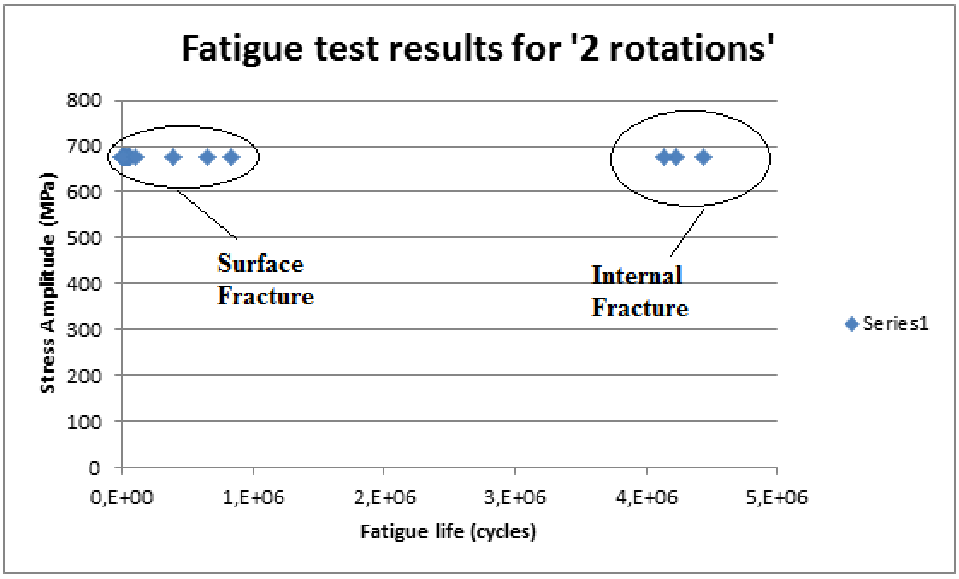

Figure 3.14: Stress amplitude as a function of fatigue life for ‘2 rotations’.

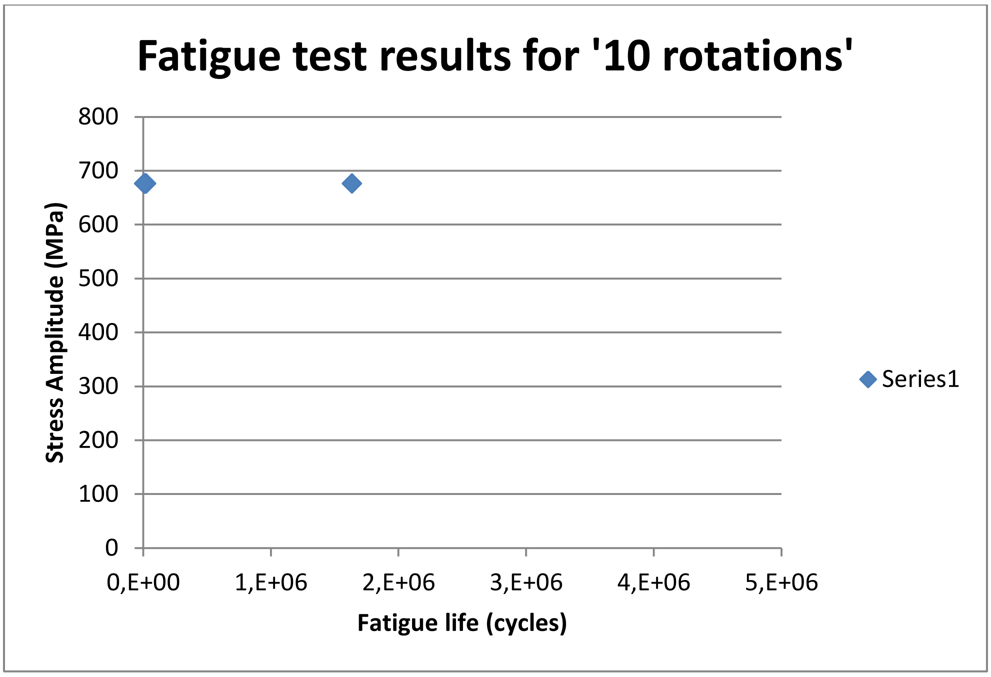

Figure 3.15: Stress amplitude as a function of fatigue life for '10 rotations'.

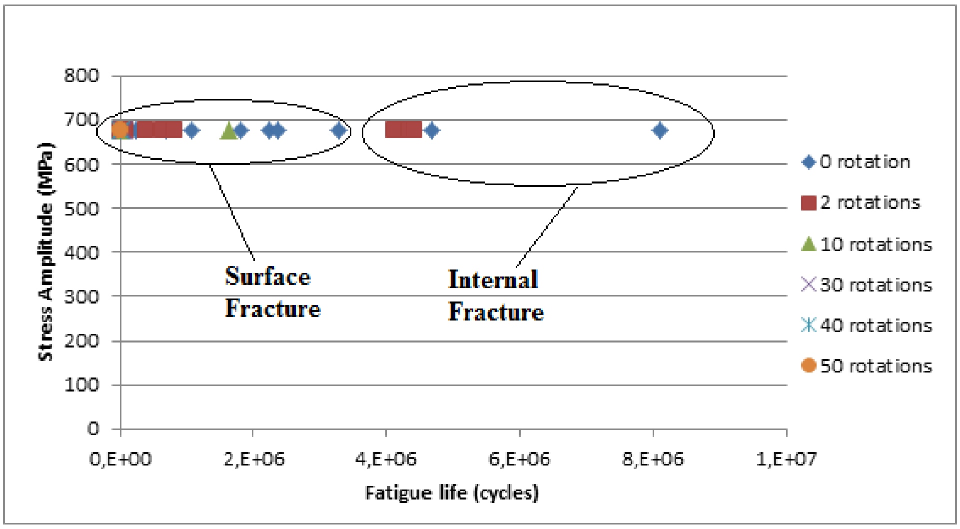

Figure 3.16: Stress amplitude as a function of cycles for various rotations.

From the figure 3.16 it is apparent that the fatigue life of heavily drawn steel wire decreases by increasing the number of rotations. It is important to note that internal crack inititaion mechanism is only active in samples with 0 and 2 twists.

3.5.2 Fractography

The fatigue fractures are positioned vertically in the vacuum chamber of the scanning electron microscope (SEM) to analyse the fracture surface of the heavily drawn steel wires (Figure 3.17).

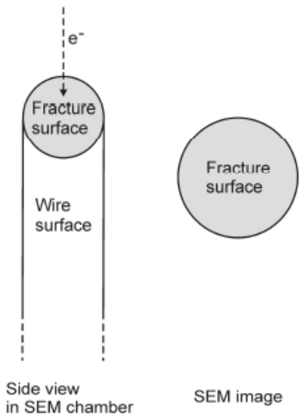

Figure 3.17: Positioning of the samples in the vacuum chamber of the SEM [1].

Surface and internal fatigue fracture modes were observed for the steel wire in this study (Figure 3.18). The fatigue cracks that initiate from surface grow semi circular and circular when the fatigue cracks initiate internally.

Surface fracture modes mostly lead to low cycle fatigue lives and the internal fracture modes lead to high cycle fatigue lives. Enviromental interaction can have an effect on surface crack inititaions, therefore surface crack inititaions are most critical mechanisms for the steel wire. A characteristic area namely the optically dark area, was observed on the fracture surface of the sample which fractured internally. It is important to note that this characterisitc area was observed only in the samples which reached above the 3 millions cycle fatigue lives. No enviromentally assisted crack initiation affects this internal fracture mode, because the fatigue crack is located completely inside the metal.

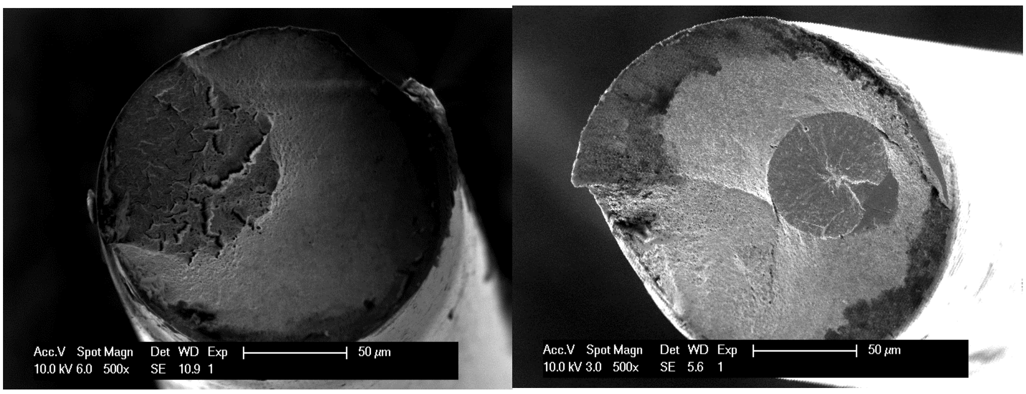

Figure 3.18: Fracture modes: (a) Surface crack. (b) Internal crack.

The internal fatigue crack which initiated at internal inclusion can be seen in Figure 3.19. From the figure it is apparent that the roughness area around the inclusion is significantly higher than the normal fracture surface. It is well known that this fatigue crack type is associated with the growth of internal short fatigue cracks.

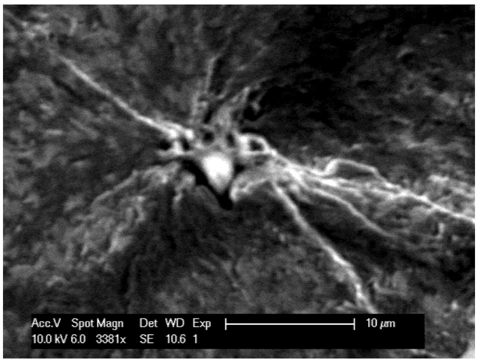

Figure 3.19: Internal crack inititaion at a non-metallic inclusion.

It can be seen from the Figure 3.20 that a lot of secondary cracks that have wavy shape are present at the fracture surface. It is most probable that the secondary cracks are formed on pearlite grain boundaries during the fatigue growth because the pearlite colonies and the secondary cracks both have the same wavy form. The stresses at the crack tip increases with increasing the size of the fatigue crack. Due to this fact the secondary cracks become deeper. The fatigue fracture plane is not completely flat but jumps down and up at secondary cracks because the growth of the cracks occurs where the resistance against the crack growth is minimum (slip planes, grain boundaries or pre existing microcracks).

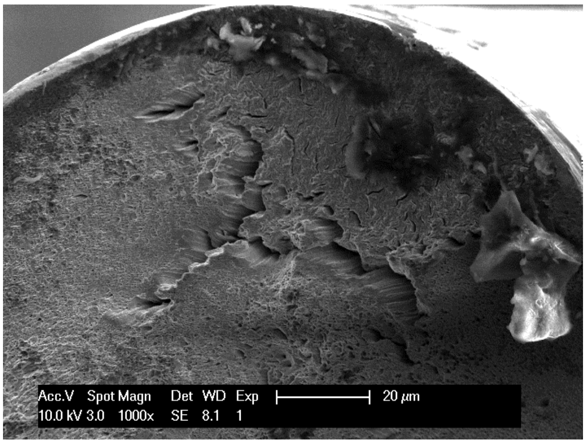

Figure 3.20: Secondary cracks at the fracture surface.

The short fatigue cracks do not propagate only on a plane perpendicular to the wire axis but also on planes in a random way and contributing to the rough surface around the non-metallic inclusion of the facet area. K.Lambrighs [1] calculated the smallest angle between the short fatigue crack and the wire axis for the drawn steel wires (same sample as the wires investigated in this study). Zelin [2] also measured the angle between between microscopic shear bands and the wire axis for drawn steel wires with a total strain of 3.5 (which is the same strain in this study). The measurement of K.Lambrighs's is 28° and Zelin's is between 30 and 45 degrees. Therefore, the short cracks grow via microscopic shear bands in the some parts of the facet area. In the other parts of the facet area, the cracks grow via grain boundaries or other low energy paths.

3.5.3 Conclusions

Based on the experimental fatigue data for heavily drawn steel wire the influence of the torsion on the fatigue properties and the active fatigue mechanisms are investigated. Due to the SEM analysis, two fracture modes were observed namely surface crack inititaion and internal crack inititaion. The cracks that initiated from the surface lead to low cycle fatigue lives and the sample that fractures internally shows characteristic area called optical dark area and leads to high cycle fatigue.

Low cycle fatigue lives were observed with increasing the number of rotations. It is important to note that the characteristic area (optical dark area) that associated with internal fracture mode was observed when the number of cylces reached above 3 million. It is apparent from the fatigue test results that the surface fracture mode is active for the heavily drawn steel wires and mostly low cycle fatigue lives are observed under mode I+III.

4. GENERAL CONCLUSIONS

Based on the mechanical test results the influence of steady torsion on the mechanical properties of heavily drawn steel wires are determined. Tensile tests, hardness tests and fatigue tests were performed with different amount of torsion to understand the torsion effect on both of static and cyclic properties of heavily drawn steel wires with a diameter of 175 μm.

According to the tensile test results, the tensile strength decreases and the ductility increases with increasing the amount of torsion. Cup-and-cone tensile fracture and dimples which are asscociated with ductile materials were observed on the fracture surface of the samples that were subjected to tensile test under pure mode I and mixed mode I+III.

The hardness test values showed that the hardness values are not proportional with the torsional deformation and for the sample subjected to twisting 20 times, the lowest hardness values were observed.

Based on experimental fatigue data two different fracture modes namely surface and internal fatigue crack inititaions are active for heavily drawn steel wires under pure mode I and mixed mode I+III. When the sample subjected to twisting 2 times, no torsion effect was observed on the fatigue properties compared to pure mode I. However, the number of cycles (fatigue lives) of the samples decreased when the number of rotations were more than 2 times. Only cracks that initiated from the surface leading to low cycle fatigue lives were found. No internal cracks were observed in sample with more than 2 twists.

REFERENCES

[1] **Kasper Lambrighs.** Fatigue properties of heavily drawn steel wires, PhD study, Katholieke Universiteit Leuven, 2010.

[2] **M.Elices.** Influence of residual stresses in the performance of cold-drawn pearlitic wires, Journal of Materials Science 39 (2004) 3889 – 3899.

[3] **X. Zhang, A. Godfrey, N. Hansen, X. Huang, W. Liu, Q. Liu**. Evolution of cementite morphology in pearlitic steel wire during wet wire drawing, Materials Characterization 61 (2010) 65-72.

[4] **M. Zelin**, Microstructure evolution in pearlitic steels during wire drawing, Acta Materialia 50 (2002) 4431–4447.

[5] **G. Sevillano, P. Van Houtte, E. Aernoudt**. large strain work hardening and textures, Progress in Materials Science AQ25(2-4) 69-412 (1980).

[6] **Montesin T, Heizmann JJ, Abdellaoui A, Pelletier JB**. Wire J Int 4 (1993) 163.

[7] **W. J. Nam, C. M. Bae, S. J. Oh, S.J. Kwon**. Effect of interlamellar spacing on cementite dissolution during wire drawing of pearlitic steel wires, Scripta mater. 42 (2000) 457–463.

[8] **V.G. Gavriljuk**. Decomposition of cementite in pearlitic steel due to plastic Deformation, Materials Science and Engineering A345 (2003) 81-89.

[9] **M. H. Hong, W. T. Reynolds, T. Tarui and K. Hono**. Atom Probe and Transmission Electron Microscopy Investigations of Heavily Drawn Pearlitic Steel Wire, Metallurgical and Materials Transactions A Vol 30 No 3 (1999) 717-727.

[10] **W. J. Nam, C. M. Bae, S. J. Oh, S.J. Kwon**. Effect of interlamellar spacing on cementite dissolution during wire drawing of pearlitic steel wires, Scripta mater. 42 (2000) 457–463.

[11] **K. Hono, M. Ohnuma, M. Murayama, S. Nishida, A. Yoshie and T. Takahashi**. Cementite decomposition in heavily drawn pearlitic steel wire, Scripta mater. 44 (2001) 977–983.

[12] **K. Van Acker, J. Root, P. Van Houtte, E. Aernoudt**. Neutron diffraction measurements of the residual stress in the cementite and ferrite phases of cold drawn steel wires, Acta Mater. Vol. 44, No. 10 (1996) 4039-4049

[13] **M. Elices**. Influence of residual stresses in the performance of cold-drawn pearlitic wires, Journal of Materials Science 39 (2004) 3889 – 3899.

[14] **F. Yang, J.Q. Jiang, F. Fang, Y. Wang, C. Ma**. Rapid determination of residual stress profiles in ferrite phase of cold drawn wire by XRD and layer removal technique, Materials science and engineering A 486 (2008) 455-460.

[15] **ASM Handbook, Volume 9**. Metallography and Microstructures, Edited by: Vander Voort, George F. ©2004 ASM International.

[16] **J.Qıan and A. Fatemi**. Mixed mode fatigue crack growth-Literature survey. Engineering Fracture Mechanics Vol.55 No.6,(1996) 969-990.

[17] **J.R. Yates, M.Zanganeh, R.A. Tomlinson, M.W.Brown, F.A.Diaz Garrido**. Crack paths under mixed mode loading, Engineering Fracture Mechanics, Internal conference of crack paths, Volume 75 (2008) 319-330.

[18] **Murakami Y., Kodama S., Konuma S**. Quantitative evaluation of non-metallic inclusions on fatigue strength of high strength steels. I: Basic fatigue mechanism and evaluation of correlation between the fatigue fracture stress and the size and location of non-metallic inclusions. Int J Fatigue 11 (1989) 291-98.

[19] **P.C. Paris, M.P. Gomez, and W.E. Anderson**. A rational analytic theory of fatigue. The Trend in Engineering 13 (1961) 9-14.

[20] **Hourlier, F. and Pineau**. A., Propagation of fatigue cracks under polymodal loading. Fatigue Fracture Engng Material Structures, 1982, 5, 287-302.

[21] **Tschegg, E.K., Stanzl, S.E.Mayer, H. R. And Czegley, M**. Crack face interactions and near-threshold fatigue crack growth. Fatigue Fracture Engng Material Structures, 1992, 16, 71-83.

[22] **M.Fonte, L.Reis, F.Romerio, B.Li, M.Freitas**. The effect of steady torsion on the fatigue crack growth in shafts, International Journal of fatigue 28, (2006) 609-617.

APPENDICES

APPENDIX A: Tensile test results

APPENDIX B: Hardness test results

APPENDIX C: Fatigue test results

APPENDIX A

Table A.1: Overview of tensile test results for 0 rotation.

Test Number	Rotations	Number of turns after sample released	Test Rate, r (mm/min)	L_0 (mm)	L_f (mm)	Diameter, D_0 (mm)	Max. Tensile load, P (N)	Modulus of Elasticity, E (GPa)	Engineering ultimate stress, S (MPa)	Engineering max. Strain, e (%)	True ultimate strength, σ (MPa)	True max. Strain, ε (%)
0.1	0	0	0,5	51,85	53,17	0,175	77,47	176	3227	2,60	3309	2,56
0.2	0	0	0,5	47,11	48,11	0,175	72,85	159	3031	2,20	3096	2,17
0.3	0	0	0,5	49,29	50,44	0,175	76,50	173	3188	2,37	3262	2,34
0.4	0	0	0,5	48,86	49,93	0,175	74,35	175	3098	2,22	3167	2,20
0.5	0	0	0,5	51,49	52,60	0,175	75,26	159	3136	2,41	3210	2,38
Average	***0***	***0***	***0,5***	-	-	***0,175***	***75,29 ±1,36***	***168 ±7,5***	***3136 ±57,2***	***2,48 ±0,12***	***3209 ±61,8***	***2,33 ±0,12***

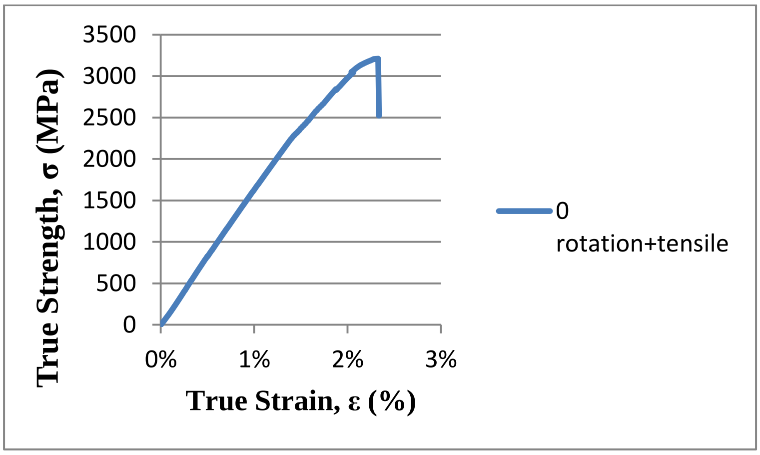

Figure A.1: True stress versus true strain curve for '0 rotation tensile test'.

Table A.2: Overview of tensile test results for 10 rotations.

Test Number	Rotations	Number of turns after sample released	Test Rate, r (mm/min)	L_0 (mm)	L_f (mm)	Diameter, D_0 (mm)	Max. Tensile load, P (N)	Modulus of Elasticity, E (GPa)	Engineering ultimate stress, S (MPa)	Engineering max. Strain, e (%)	True ultimate strength, σ (MPa)	True max. Strain, ε (%)
10a.1	10	0	0,5	50,46	52,09	0,175	70,57	156	2940	3,52	3034	3,46
10a.2	10	0	0,5	51,55	53,01	0,175	69,93	149	2813	3,18	2895	3,13
10a.3	10	0	0,5	50,67	52,22	0,175	74,22	171	2839	2,06	2897	2,04
10a.4	10	0	0,5	52,42	53,71	0,175	63,58	169	2649	2,20	2714	2,23
Average	***10***	***0***	***0.5***	-	-	***0,175***	***69,57 ±3***	***161 ±8,7***	***2810,25± 80***	***2,74 ±0,6***	***2885 ±85***	***2,72 ±0,6***
10b.1	10	2	0,5	50,73	52,03	0,175	73,12	169	3046	2,60	3124	2,57
10b.2	10	1	0,5	52,07	53,30	0,175	67,16	163	2796	2,40	2864	2,38
10b3	10	1	0,5	50,67	52,22	0,175	74,22	171	3093	3,05	3187	3,01
10b.4	10	2	0,5	53,21	54,65	0,175	71,83	160	2993	2,72	3073	2,68
10b.5	10	1	0,5	52,55	53,70	0,175	66,25	164	2761	2,26	2821	2,20
10b.6	10	2	0,5	50,61	52,04	0,175	73,08	154	3045	3,18	3131	3,13
Average	-	-	***0,5***	-	-	***0,175***	***70,94 ±3,16***	***163,5 ±3,2***	***2955,67 ±127***	***2,70 ±0,3***	***3033,3 ±128***	***2,66 ±0,3***

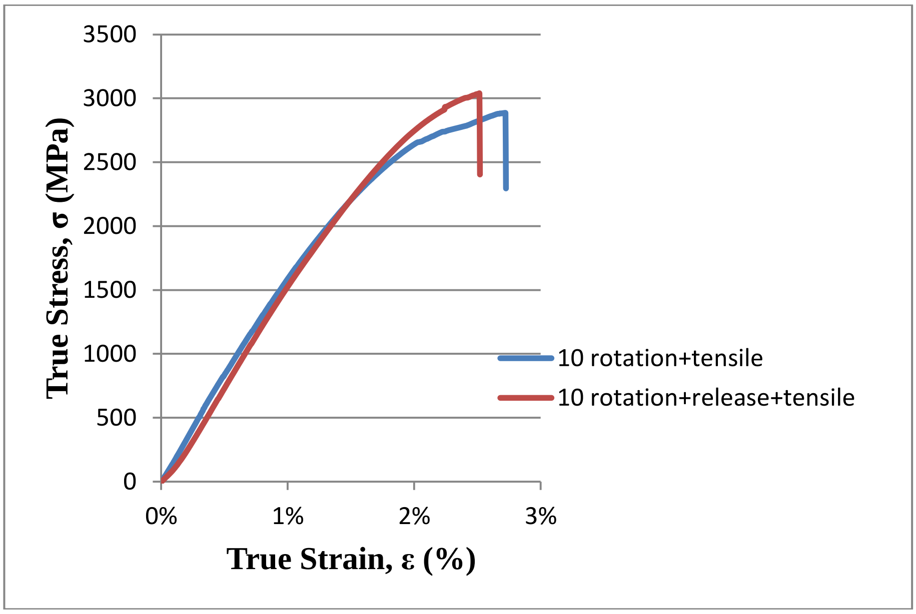

Figure A.2: True stress versus strain curves for '10'rotations.

Table A.3: Overview of tensile test results for 20 rotations.

Test Number	Rotations	Number of turns after sample released	Test Rate, r (mm/min)	L_0 (mm)	L_f (mm)	Diameter, D_0 (mm)	Max. Tensile load, P (N)	Modulus of Elasticity, E (GPa)	Engineering ultimate stress, S (MPa)	Engineering max. Strain, e (%)	True ultimate strength, σ (MPa)	True max. Strain, ε (%)
20a.1	20	0	0,5	53,02	54,72	0,175	72,03	167	2998	3,22	3094	3,17
20a.2	20	0	0,5	53,02	54,94	0,175	71,62	173	2983	3,66	3090	3,59
20a.3	20	0	0,5	49,67	51,46	0,175	71	153	2958	3,66	3064	3,60
20a.4	20	0	0,5	49,50	51,46	0,175	71,83	166	2992	3,96	3111	3,89
20a.5	20	0	0,5	50,19	51,86	0,175	68,90	143	2869	3,35	2964	3,29
20a.6	20	0	0,5	50,19	52,14	0,175	70,81	138	2916	4,20	3034	4,12
Average	*20*	*0*	*0,5*	-	-	*0,175*	*71,03 ±0,96*	*157 ±10*	*2953±40*	*3,62 ±0,25*	*3059 ±42*	*3,6 1±0,25*
20b.1	20	1	0,5	52,70	54,74	0,175	72	176	2998	3,90	3114	3,82
20b.2	20	2	0,5	54,11	55,75	0,175	71,88	163	2995	3,08	3085	3,03
20b.3	20	3	0,5	50,75	52,08	0,175	71,28	172	2970	2,66	3048	2,63
20b.4	20	2	0,5	50,79	52,53	0,175	72	169	3002	3,47	3148	3,42
20b.5	20	2	0,5	48,38	49,83	0,175	72,23	172	2966	3,02	3055	2,98
Average	*20*	-	*0,5*	-	-	*0,175*	*71,03 ±0,28*	*157 ±3*	*2986,2 ±15*	*3,23 ±0,2*	*3090 ±32*	*3,18 ±0,2*

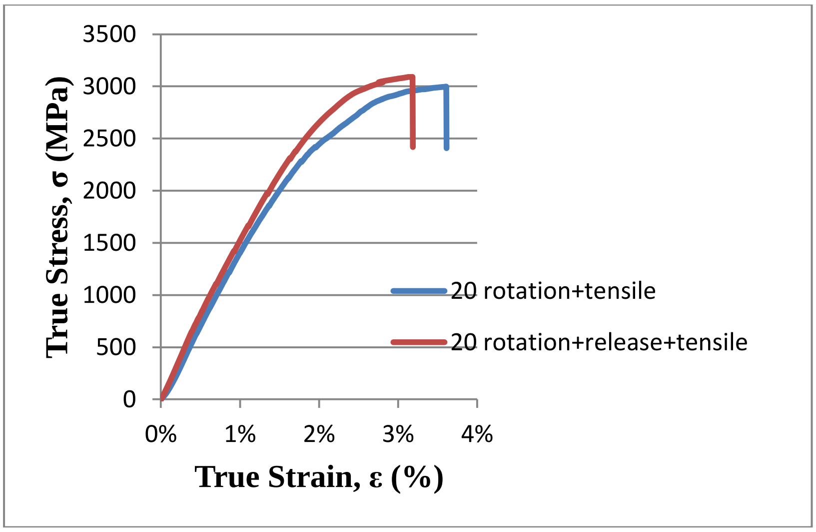

Figure A.3: True stress versus true strain curves for ‘20’rotations.

Table A.4: Overview of tensile test results for 30 rotations.

Test Number	Rotations	Number of turns after sample released	Test Rate, r (mm/min)	L_0 (mm)	L_f (mm)	Diameter, D_0 (mm)	Max. Tensile load, P (N)	Modulus of Elasticity, E (GPa)	Engineering ultimate stress, S (MPa)	Engineering max. Strain, e (%)	True ultimate strength, σ (MPa)	True max. Strain, ε (%)
30a.1	30	0	0,5	51,68	53,71	0,175	70,07	149	2919	3,93	3034	3,86
30a.2	30	0	0,5	52,59	54,25	0,175	71,35	166	2970	3,16	3064	3,11
30a.3	30	0	0,5	52,55	54,48	0,175	70,53	175	2937	3,67	3045	3,60
30a.4	30	0	0,5	50,40	51,91	0,175	66,73	160	2770	3,01	2852	2,96
30a.4	30	0	0,5	50,03	51,70	0,175	69,22	173	2869	3,36	2965	3,31
30a.5	30	0	0,5	52,47	54,30	0,175	69,09	138	2877	3,79	2979	3,72
Average	***30***	***0***	***0,5***	-	-	***0,175***	***70,05 ±1,5***	***160,2 ±5,5***	***2890,3 ±55,12***	***3,49 ±0,26***	***2989,8 ±59***	***3,43 ±0,26***
30b.1	30	2	0,5	45,11	46,63	0,175	70,90	152	2953	3,41	3052	3,36
30b.2	30	3	0,5	48,03	49,62	0,175	70,87	175	2948	3,34	3046	3,29
30b.3	30	2	0,5	51,86	53,43	0,175	70,28	169	2926	3,06	3014	3,01
Average	***30***		***0,5***	-	-	***0,175***	***70,7±0,3***	***161,2±3***	***2942,3±11***	***3,27±0,14***	***3037,3±16***	***3,22±0,14***

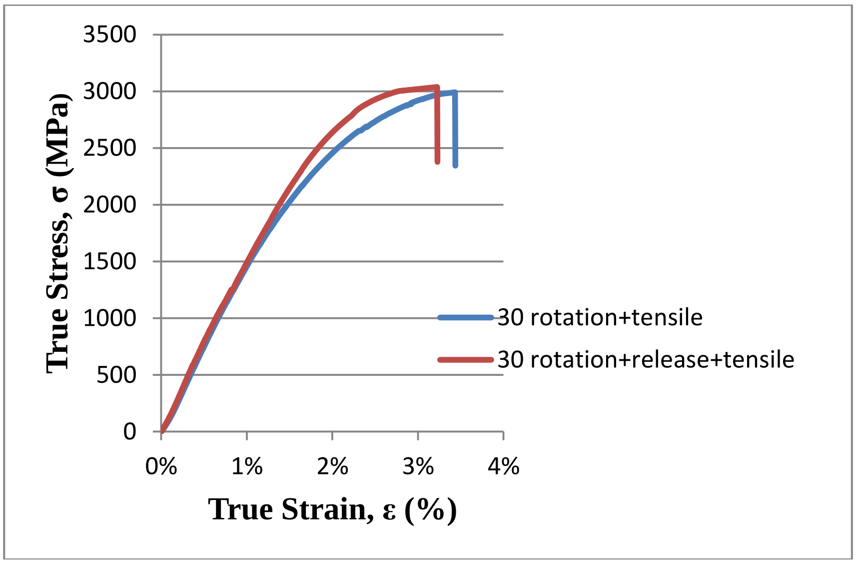

Figure A.4: True stress versus strain curves for '30'rotations.

Table A.5: Overview of tensile test results for 40 rotations.

Test Number	Rotations	Number of turns after sample released	Test Rate, r (mm/min)	L_0 (mm)	L_f (mm)	Diameter, D_0 (mm)	Max. Tensile load, P (N)	Modulus of Elasticity, E (GPa)	Engineering ultimate stress, S (MPa)	Engineering max. Strain, e (%)	True ultimate strength, σ (MPa)	True max. Strain, ε (%)
40a.1	40	0	0,5	47,81	49,69	0,175	68,75	168	2865	3,96	2976	3,88
40a.2	40	0	0,5	51,50	53,60	0,175	68,66	177	2861	3,82	2976	3,75
40a.3	40	0	0,5	48,30	50,41	0,175	69,05	164	2877	4,10	3003	4,01
40a.4	40	0	0,5	47,58	49,49	0,175	68,69	167	2862	4,04	2977	3,96
40a.5	40	0	0,5	51,34	53,11	0,175	68,03	146	2834	3,78	2948	3,70
Average	***40***	***0***	***0,5***	-	-	***0,175***	***68,6±0,29***	***164±8,8***	***2859,8±12***	***3,94±0,13***	***2976±14***	***3,86±0,13***
40b.1	40	2	0,5	45,66	46,76	0,175	63,65	155	2652	2,42	2716	2,39
40b.2	40	3	0,5	53,05	54,25	0,175	63,26	151	2635	2,28	2693	2,26
40b.3	40	1	0,5	52,14	54,17	0,175	70	175	2918	3,93	3031	3,86
40b.4	40	2	0,5	47,15	49,16	0,175	69,81	167	2906	3,65	3011	3,58
40b.5	40	2	0,5	44,07	45,65	0,175	69,61	165	2899	3,65	3003	3,58
Average	***40***	-	***0,5***	-	-	***0,175***	***67,3±2,46***	***163±6,8***	***2802±102***	***3,19±0,55***	***2890,8±120***	***3,13±0,53***

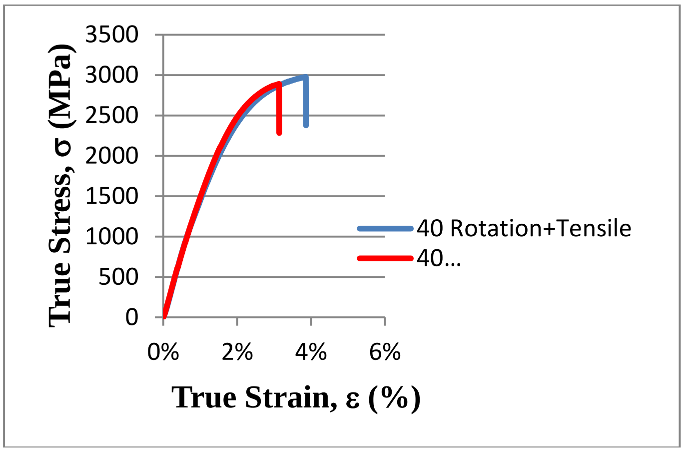

Figure A.5: True stress versus strain curves for '40'rotations.

Table A.6: Overview of tensile test results for 50 rotations.

Test Number	Rotations	Number of turns after sample released	Test Rate, r (mm/min)	L_0 (mm)	L_f (mm)	Diameter, D_0 (mm)	Max. Tensile load, P (N)	Modulus of Elasticity, E (GPa)	Engineering ultimate stress, S (MPa)	Engineering max. Strain, e (%)	True ultimate strength, σ (MPa)	True max. Strain, ε (%)
50a.1	50	0	0,5	49,95	52,38	0,175	68,83	174	2868	4,22	2998	4,13
50a.2	50	0	0,5	54,64	56,54	0,175	68,08	178	2834	3,50	2932	3,44
50a.3	50	0	0,5	49,89	51,94	0,175	68,70	175	2709	3,27	2796	3,22
50a.4	50	0	0,5	50,44	52,01	0,175	66,36	177	2858	4,16	2975	4,07
50a.5	50	0	0,5	51,29	52,88	0,175	64,48	140	2764	3,19	2850	3,14
Average	**50**	**0**	**0,5**	-	-	**0,175**	**67,29±1,49**	**169±15**	**2684±55**	**3,41±0,3**	**2781±65**	**3,36±0,3**
50b.1	50	2	0,5	45,80	47,16	0,175	66,56	149	2773	3,02	2857	2,97
50b.2	50	2	0,5	46,93	48,91	0,175	69,71	164	2902	4,26	3025	4,17
50b.3	50	3	0,5	44,77	46,49	0,175	69,77	172	2903	3,88	3015	3,80
50b.4	50	3	0,5	48,53	50,13	0,175	69,27	171	2535	2,34	2594	2,31
Average	***50***	-	***0,5***	-	-	***0,175***	***68,82±0,2***	***160±3,3***	***2883±163***	***3,32±0,77***	***2978±189***	***3,27±0,74***

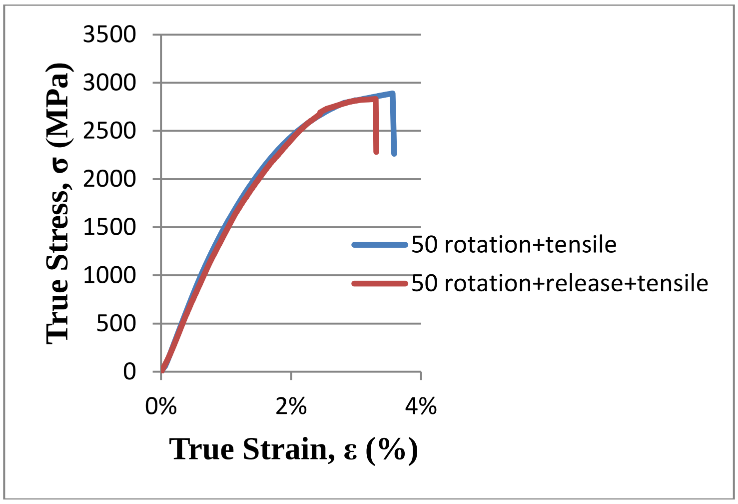

Figure A.6: True stress versus strain curves for '50'rotations.

APPENDIX B

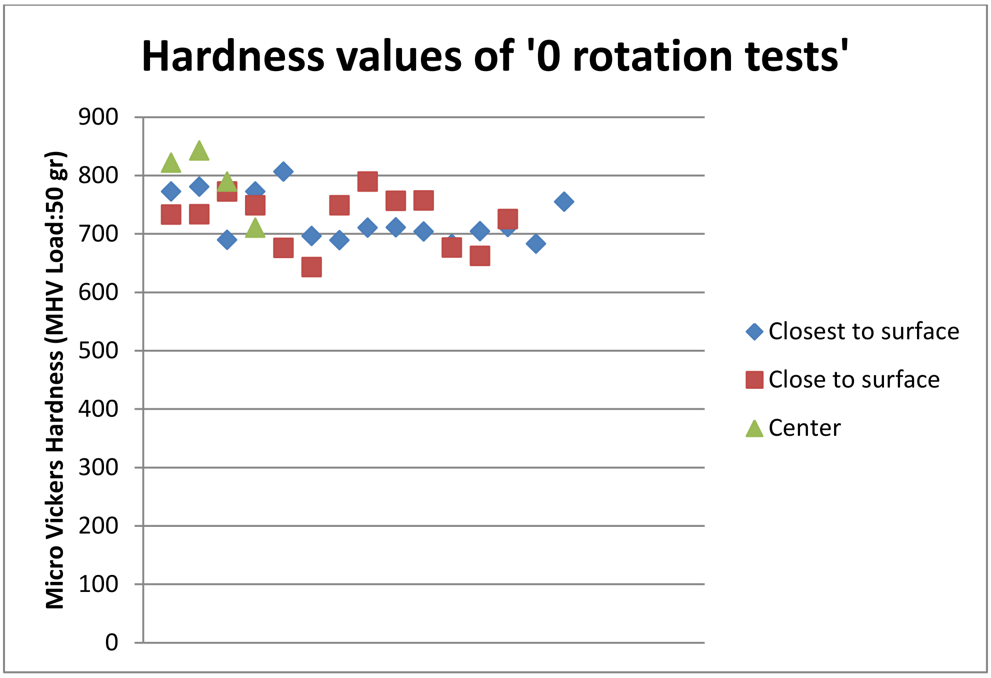

Figure B.1: The hardness values of ‘0 rotation tests’.

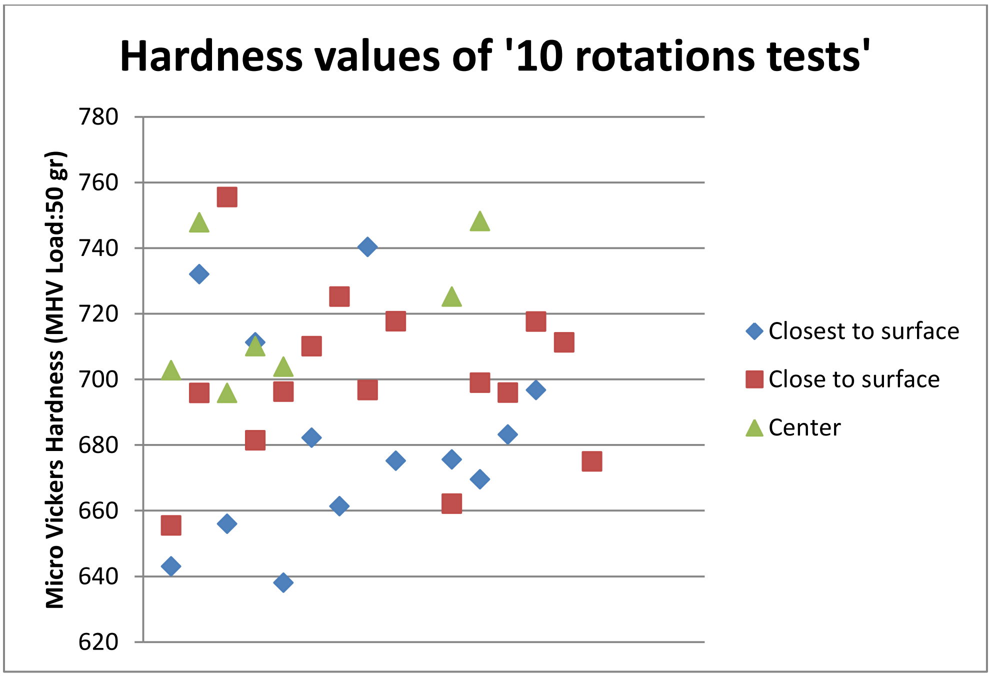

Figure B.2: The hardness values of ’10 rotations tests’.

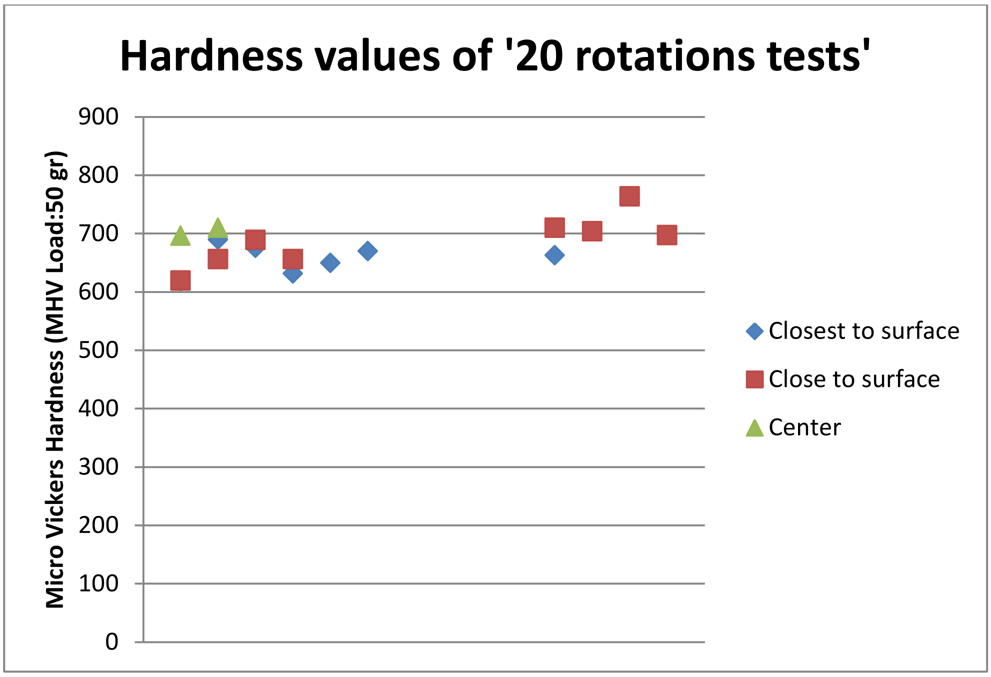

Figure B.3: The hardness values of ’20 rotations tests’.

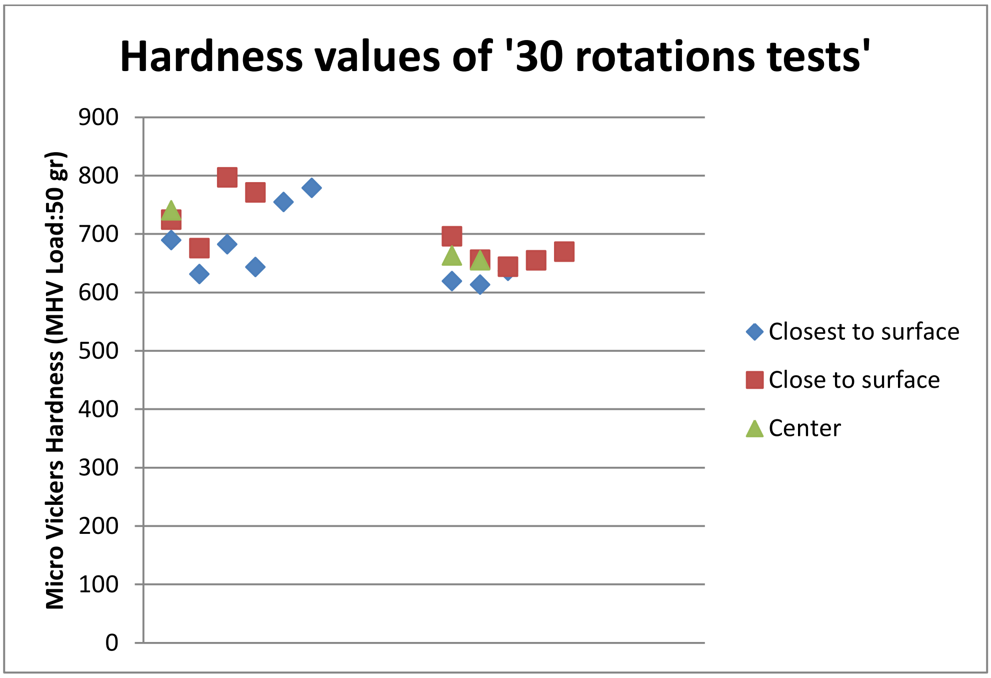

Figure B.4: The hardness values of ’30 rotations tests’.

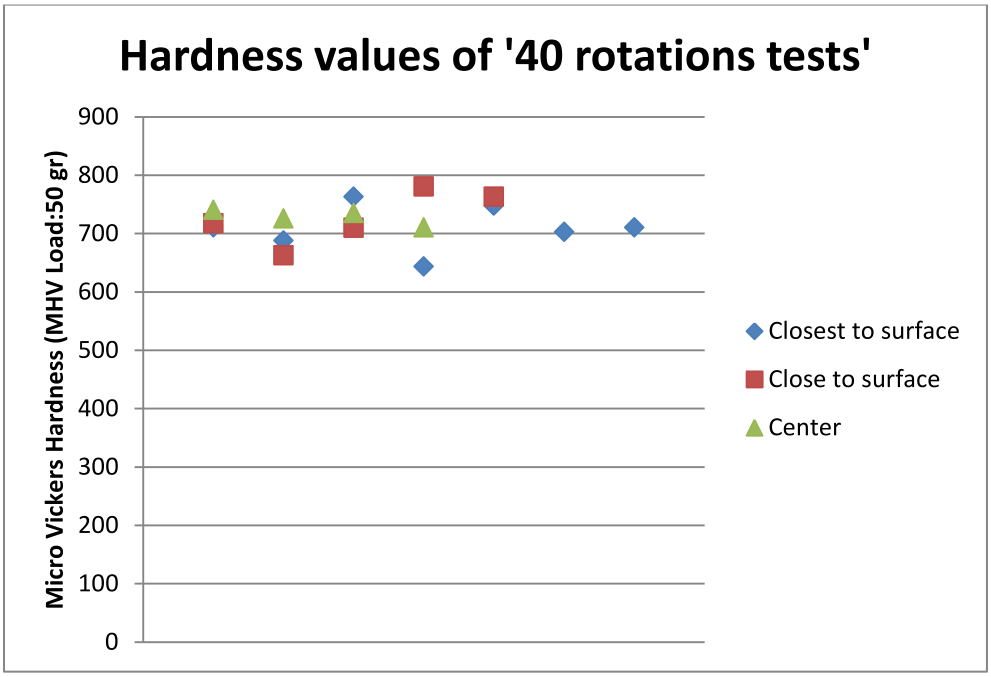

Figure B.5: The hardness values of '40 rotations tests'.

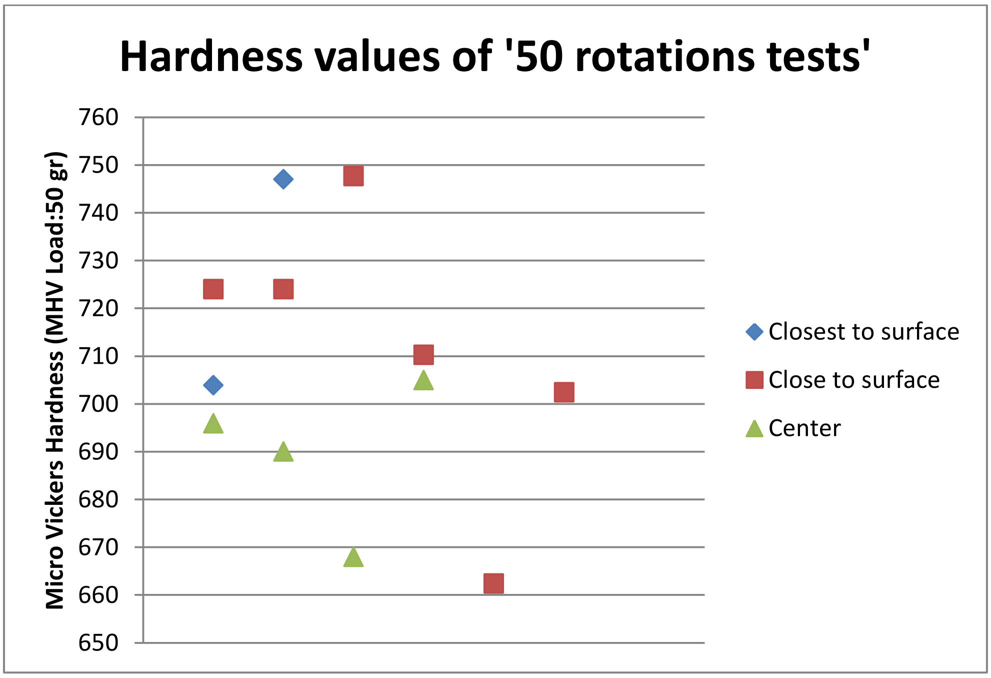

Figure B.6: The hardness values of '50 rotations tests'.

APPENDIX C

Table C.1: The fatigue tests results for different amount of torsion.

Sample No	Gauge Length (cm)	Number of twists	Fatigue life (Number of cycles)	Fracture mode	Fracture place
1	54,90	0	2,235,660	Surface	Near the clamps
2	51,8	0	4,667,189	Internal	Near the Center
3	54,77	0	13,933	Surface	Near the clamps
4	52,72	0	1,082,960	Surface	Near the clamps
5	53,45	0	98,033	Surface	Near the Center
6	51,74	0	237,396	Surface	Near the Center
7	51,79	0	32,552	Surface	Near the clamps
8	54,80	0	697,735	Surface	Near the clamps
9	54,24	0	123,714	Surface	Near the center
10	53,80	0	19,036	Surface	Near the clamps
11	51,50	0	229,976	Surface	Near the clamps
12	50,39	0	3,286,287	Internal	Near the center
13	51,16	0	1,811	Surface	Near the clamps
14	51,20	0	8,104,754	Internal	Near the clamps
15	51,23	2	10,092	Surface	Near the clamps
16	51,70	2	13,807	Surface	Near the clamps
17	52,30	2	51,280	Surface	Near the clamps
18	51,45	2	394,297	Surface	Near the clamps
19	52,72	2	20,242	Surface	Near the clamps
20	52,12	2	655,657	Surface	Near the clamps
21	53,46	2	32,121	Surface	Near the clamps

22	52,90	2	51,818	Surface	Near the clamps
23	53,10	2	54,394	Surface	Near the clamps
24	53,28	2	28,125	Surface	Near the clamps
25	51,20	2	4,231,987	Internal	Near the center
26	52,30	2	35,618	Surface	Near the clamps
27	53,15	2	28,408	Surface	Near the center
28	52,60	2	57,144.	Surface	Near the clamps
29	55	2	4,438,234	Internal	Near the center
30	53,40	2	621,187	Surface	Near the clamps
31	49,10	2	835,196	Surface	Near the center
32	57,60	2	4,129,399	Internal	Near the clamps
33	54,15	2	14,554	Surface	Near the clamps
34	51,46	2	97,497	Surface	Near the clamps
35	52,25	10	13,323	Surface	Near the center
36	53,35	10	23,112	Surface	Near the center
37	57,80	10	1,636,661	Surface	Near the center
38	53,30	10	13,119	Surface	Near the center
39	49,10	10	18,083	Surface	Near the center
40	50,60	10	12,881	Surface	Near the center
41	51,35	20	235,470	Surface	Near the clamps
42	52,70	20	33,026	Surface	Near the clamps
43	51,47	20	839,006	Surface	Near the center
44	52,20	30	50,034	Surface	Near the clamps
45	52,80	30	20,156	Surface	Near the clamps
46	51,90	30	25,065	Surface	Near the clamps
47	50,27	30	237,063	-	Near the clamps
48	53,40	40	11,945	-	Near the clamps

49	51,16	40	6,880	-	Near the clamps
50	50,65	40	9,046	-	Near the clamps
51	51,55	40	4,655	-	Near the clamps
52	52,61	50	11,781	-	Near the center
53	50,25	50	6,706	-	Near the clamps
54	53,67	50	6,257	-	Near the clamps
55	50,47	50	3,867	-	Near the clamps
56	50,55	50	9,445	-	Near the clamps

CURRICULUM VITAE

Name Surname: Gökay BARANOĞLU

Place and Date of Birth: İstanbul / 13.06.1986

Address: Mareşal Çakmak Mah. Mercan Sok. Ortaç Cad. No: 22/10 Güngören/İstanbul

E-Mail: gokaybaranoglu@gmail.com

B.Sc.: Yıldız Technical University /Metallurgical and Materials Engineering

M.Sc.: Istanbul Technical University / Materials Engineering